Article

Not peer-reviewed version

New Decomposition Models for Hourly Direct Normal Irradiance Estimations for Southern Africa

Francisca Muriel Daniel-Durandt and Arnold Johan Rix *

Posted Date: 7 March 2024

doi: 10.20944/preprints202403.0416.v1

Keywords: Decomposition Model; Global Horizontal Irradiance; Direct Normal Irradiance; Solar Radiation Model

Preprints.org (www.preprints.org) | NOT PEER-REVIEWED | Posted: 7 March 2024 doi:10.20944/preprints202403.0416.v1

Article

New Decomposition Models for Hourly Direct Normal Irradiance Estimations for Southern Africa

Francisca Muriel Daniel-Durandt † and **Arnold Johan Rix** *,†

Stellenbosch University; 18296033@sun.ac.za
* Correspondence: rix@sun.ac.za
† These authors contributed equally to this work.

Abstract: The research develops and validates new decomposition models for DNI estimations from Southern African data. The results demonstrated improved DNI estimation accuracy compared to the baseline models across all testing and validation datasets. These outcomes suggest that utilising a localised model can significantly enhance DNI estimations for Southern Africa and potentially for developing similar models in diverse geographic regions worldwide. Furthermore, clustered models highlighted the potential advantages of grouping data based on shared geographical and climatic attributes. This clustering approach could enhance decomposition model performance, particularly when local data is limited or data is available from multiple nearby stations. The Southern African decomposition model, which encompasses a wide spectrum of climatic regions and geographic locations, exhibited notable improvements over the baseline models despite occasional overestimation or underestimation. The overall metrics affirm the substantial advancement achieved with the Southern African model. This study focused on validating the model for hourly DNI in Southern Africa within a range of K_t-intervals from 0.175 to 0.875. Implementing accurate decomposition models in developing countries can accelerate the adoption of renewable energy sources, diminishing reliance on coal and fossil fuels.

Keywords: decomposition model; global horizontal irradiance; direct normal irradiance; solar radiation model

---

1. Introduction

Photovoltaic (PV) systems require accurate modelling and monitoring to ensure their profitability. The amount of irradiance at the site, the GPI, is the foundation of designing, modelling and monitoring PV systems. The global plane-of-array irradiance (GPI) comprises the plane-of-array's (POA) direct beam, ground and diffuse irradiance components. GPI is used to model and monitor PV systems, as this shows the amount of generated solar power and, therefore, one of the most important contributing factors to designing a PV system. The global horizontal irradiance (GHI), direct normal irradiance (DNI) and diffuse horizontal irradiance (DHI) components are required to calculate these irradiance components.

Irradiance components with a transposition model calculate GPI (G_{POA}) as

$$G_{POA} = G_{BC} + G_{DC} + G_{RC}. \tag{1}$$

G_{BC} is the direct beam irradiance, G_{RC} is the ground-reflected irradiance, and G_{DC} is the diffuse irradiance component in the POA. GHI, DNI and DHI components are required to calculate G_{BC}, G_{DC} and G_{RC}. The sum of the DNI projected onto the horizontal surface using the cosine of the solar zenith angle θ_Z, and DHI gives the GHI, shown in Figure 1, [1]:

$$GHI = DNI \cdot \cos\theta_Z + DHI. \tag{2}$$

 doi:10.20944/preprints202403.0416.v1

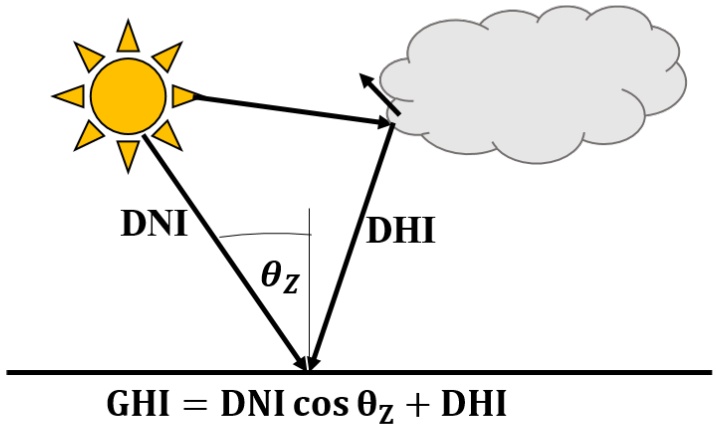

Figure 1. The irradiance relationships between GHI, DNI, DHI and θ_Z.

GHI, DHI, and DNI units are in W/m^2.

Most ground-based stations have at least measurements of GHI. Other measurements include radiometric data such as DNI, DHI and ultra-violet, and meteorologic data such as the temperature, pressure, rainfall, relative humidity, wind direction and wind speed. Pyranometers measure DHI and GHI, and the pyrheliometer measures DNI.

GHI is measured with a hemispherical view and is mounted horizontally. Similar in setup to other pyranometers, the DHI pyranometer includes the additional feature of being shaded from direct sunlight. The pyrheliometer has a narrow view that only measures the beam directly from the Sun and is usually a Sun tracker for increased accuracy [2]. The irradiance measurements are converted to W/m^2 and logged accordingly.

Calibrating the equipment to the ISO 9060:1990 standard is necessary, and it is advisable to undergo recalibration every two years to ensure the reliability of measurements. The maintenance required is to clean the domes and regularly check and replace the desiccant, which keeps the instruments dry internally.

GHI, DNI and DHI are interdependent; therefore, having only two irradiance measurements is sufficient to estimate the third using the decomposition models (also sometimes called separation models) [3]. If only the GHI is available, the DNI and DHI also are estimated using the decomposition models. The transposition models calculate GPI using the irradiance components. Therefore, GHI, DHI and DNI correlations are usually empirically expressed as a decomposition model [4].

Indices are relationships between different irradiance components. Decomposition and transposition models utilise these relationships.

The definition of the direct beam transmittance K_n and diffuse transmittance K_d is

$$K_n = \frac{DNI}{G_{0n}}, \tag{3}$$

$$K_d = \frac{DHI}{GHI}. \tag{4}$$

Liu and Jordan defined the K_t as

$$K_t = \frac{GHI}{G_{0n}\cos\theta_Z}. \tag{5}$$

All K-values (K_t, K_n and K_d) are unitless.

The extraterrestrial irradiance on a normal surface G_{0n} depends on the day of the year

$$G_{0n} = (\text{Solar Constant})\left(1 + 0.033 \cdot \cos\left(\frac{360 \cdot n}{365}\right)\right). \tag{6}$$

The Solar Constant is usually 1,367 W/m^2.

Determining the horizontal extraterrestrial irradiance G_{0h} involves multiplying it by the cosine of θ_Z as expressed in Equation (7):

$$G_{0h} = G_{0n} \cdot \cos \theta_Z. \tag{7}$$

Multipredictor decomposition models can improve accuracy compared to single predictor models [6]. However, the disadvantage is that multiple measurements must be available, which is not always the case for developing countries or brand-new sites of PV installations.

Boland *et al.* and Ridley *et al.* developed a logistical model to estimate solar diffuse radiation [7,8]. Soares *et al.*, Talvitie *et al.*, and Kalyanam and Hoffmann have proposed machine-learning-based models to predict solar diffuse and direct components [9–11]. Bessafi *et al.* have proposed a satellite-based decomposition model as an alternative to ground-based measurements [12], and Janjai *et al.* have proposed statistical models for estimating diffuse radiation [13].

Decomposition models have been developed by assessing previous models and improving the accuracy of these estimations. As more data and measurements become available, researchers have the opportunity to develop models for different climates and temporal resolutions. Most models predominantly use K_t. Some of the variables used in the decomposition models are the solar altitude angle β and dew point temperature T_d. Using K_t as the main predictor in decomposition models is popular because of its simplicity and applicability [6].

Orgill and Hollands developed a relationship between the K_t and K_d [14], and Erbs *et al.* extended the K_t-K_d relationship to latitudes from 31 to 42° North [15]. Louche *et al.* established a GHI and DNI relationship for a Mediterranean site to estimate K_n using K_t [16].

The Direct Insolation Simulation Code (DISC) was developed by Maxwell [17], and Perez *et al.* developed the Dirint model with the hopes of increasing the performance of the DISC model [18]. The Dirint model of Perez *et al.* has shown superior performance when estimating the DNI [19].

In Korea, Lee *et al.* developed a model using 6 Korean locations [20], and Lee *et al.* developed a new model using Maxwell's DISC model by refitting the coefficients [3]. Skartveit and Olseth developed a DNI estimation model using the solar elevation angle for Norway based on hourly GHI and DHI records [21].

Lam and Li derived K_d for Hong Kong [22]. Reindl *et al.* determined K_d using two models with K_t and β [23].

The main limitations of decomposition models are that some have limited climate scope, and the dataset's temporal resolution affects the irradiance estimation accuracy. A decomposition model in a tropical climate may be unsuitable for a desert climate and vice versa. Intra-hourly-based models perform differently from daily- or monthly-based models, which is why many available decomposition models exist.

Several regions, such as Belgium [4], China [24], the USA [19], and North Africa [25], evaluated the accuracy of decomposition models.

Gueymard and Ruiz-Arias provided an extensive study of 140 available decomposition models. The authors state that the predicted DNI's accuracy highly depends on the decomposition model. Validation studies exist but are limited to a few models and test stations, i.e. biased to a specific location or climate [26]. Research indicates that no decomposition model has been developed and validated for South Africa.

Laiti *et al.* state that, in general, decomposition models tend to overestimate DHI and underestimate DNI and typically, models tend to underestimate DHI in overcast periods and overestimate during clear-sky periods [19].

Higher resolution data include higher K_t values, resulting in extreme overestimations of DNI. These hourly DNI estimates have higher accuracy than 1-minute DNI estimates. Subhourly estimations would be highly beneficial for real-time monitoring and forecasting of solar power [26].

Figure 2 visualises the testing and validation countries of common decomposition models in green of models such as Orgill and Hollands, Erbs *et al.*, Louche *et al.*, Reindl *et al.*, DISC (Maxwell), Dirint (Perez *et al.*), Lee *et al.*, Lee *et al.*, Skartveit and Olseth and Lam and Li) [3,14–18,20–23].

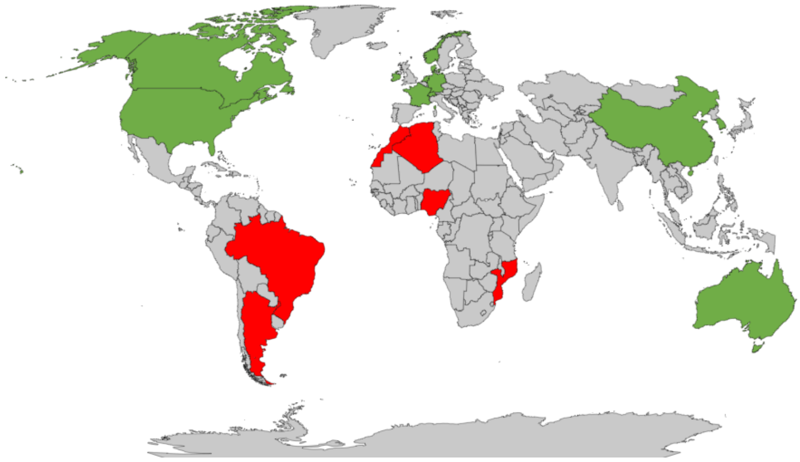

Figure 2. Validation sites of discussed decomposition models.

The development of the decomposition model in South America includes Brazil [28], Argentina and Brazil [29]. Northern African models include Nigeria [30], Algeria [31] and Morocco [32].

Engerer developed a model for Australia and observed that the model only slightly outperformed the Dirint model [33]. The BRL model by Ridley *et al.* developed a method to construct multiple variable logistic models for the diffuse solar fraction, which includes Mozambique [8]. Figure 2 represents these discussed models [8,28–33] in red.

South African research on decomposition models includes the following: Tsubo and Walker published the only Southern African-based study on the relationship between radiation and K_t [34]. However, this relationship is with photosynthetically active radiation related to agricultural practices, not PV systems. Clear-sky model assessments and validation studies have been performed by [35] and [36] for Southern African countries. Clear-sky models simplify atmospheric attenuation to estimate solar irradiance under clear-sky conditions and do not represent decomposition models and is not include these studies as comparison models, as they are irrelevant to the research.

Mahachi's thesis assessed decomposition and transposition models in South Africa and showed that the models tend to overestimate the DHI but underestimate the DNI [37]. Furthermore, the DISC and Dirint decomposition models showed the most accurate estimations of the DNI and DHI for the South African climatic conditions [38].

As discussed, decomposition models are empirical relationships between GHI, DHI and DNI. All three irradiance components are required to estimate GPI. Decomposition models are useful as it reduces the measurement equipment by decomposing one irradiance component into two other; for example, use GHI to estimate DHI and DNI.

Most decomposition models are not universally applicable and localised to a specific climate, and the temporal resolution is not always transferable. There has not been extensive literature published representing the Southern African region in decomposition models, which this research article will attempt to address.

2. Model Development

The methodology to develop a novel decomposition model is based on selected data from the automated QC procedure and addresses three geographical models:

1. a localised decomposition model, which is site-specific;
2. a clustered decomposition model, which encapsulates several sites to group an area based on their geographical location;
3. and a regional (Southern African) model, which encapsulates the data from the SAURAN network for developing a model specific to Southern Africa.

 doi:10.20944/preprints202403.0416.v1

2.1. SAURAN Database

Table 1 summarises the SAURAN stations' corresponding geographical information, such as latitude, longitude, and elevation above sea level.

Table 1. SAURAN station summary [39,40].

	Name (Location)	Coordinates (Lat (°S), Long (°E))	Elevation (m)
CSIR	CSIR Energy Centre (Pretoria, South Africa)	25.747, 28.279	1400
CUT	Central University of Technology (Bloemfontein, South Africa)	29.121, 26.216	1397
FRH	University of Fort Hare (Alice, South Africa)	32.785, 26.845	540
GRT	Graaff-Reinet (Graaff-Reinet, South Africa)	32.485, 24.586	660
HLO	Mariendal (Mariendal, South Africa)	33.854, 18.824	178
ILA	Ilanga CSP Plant (Upington, South Africa)	28.490, 21.520	884
KZH	University of KwaZulu-Natal Howard College (Durban, South Africa)	29.871, 30.977	150
KZW	University of KwaZulu-Natal Westville (Durban, South Africa)	29.817, 30.945	200
MIN	CRSES Mintek (Johannesburg, South Africa)	26.089, 27.978	1521
NMU	Nelson Mandela University (Gqeberha, South Africa)	34.009, 25.665	35
NUST	Namibian University of Science and Technology (Windhoek, Namibia)	22.565, 17.075	1683
RVD	Richtersveld (Alexander Bay, South Africa)	28.561, 16.761	141
SUN	Stellenbosch University (Stellenbosch, South Africa)	33.935, 18.867	119
UBG	Gaborone (Gaborone, Botswana)	24.661, 25.934	1014
UFS	University of Free State (Bloemfontein, South Africa)	29.111, 26.185	1491
UNV	Venda (Vuwani, South Africa)	23.131, 30.424	628
UNZ	University of Zululand (KwaDlangezwa, South Africa)	28.853, 31.852	90
UPR	University of Pretoria (Pretoria, South Africa)	25.753, 28.229	1410
VAN	Vanrhynsdorp (Vanrhynsdorp, South Africa)	31.617, 18.738	130

Table 3 shows the data points available for the model development, taken from Table 2. Further, the data points assessed are K_t between 0.175 and 0.875.

The data points are hourly measurements of the GHI, DNI and DHI. The split of the train-validation-test datasets is 50:25:25, with the exceptions of two datasets, ILA and MIN. The ILA and MIN have a 0:0:100 data split and are two unknown datasets as part of the test study.

Table 3 also shows each station's mean GHI, DNI, and DHI determined after applying the QC procedure.

Preprints.org (www.preprints.org) | NOT PEER-REVIEWED | Posted: 7 March 2024 doi:10.20944/preprints202403.0416.v1

Table 2. SAURAN database and dataset sizes from [39].

Station	Dataset size		Start Date	End Date
	Before QC	After QC		
CSIR	46,434	26,539	11 March 2017	31 October 2022
CUT	28,077	14,619	24 October 2017	31 October 2022
FRH	40,895	22,233	7 February 2017	24 February 2022
GRT	18,541	9774	27 November 2013	24 January 2016
HLO	21,532	11,728	8 October 2015	27 October 2020
ILA	8832	4676	13 October 2021	31 October 2022
KZH	52,323	38,898	7 December 2015	07 August 2022
KZW	20,291	10,756	7 December 2015	12 December 2018
MIN	8185	4423	28 October 2021	31 October 2022
MRB	4201	2462	17 March 2017	22 October 2019
NMU	39,969	23,130	10 December 2015	30 September 2022
NUST	52,004	27,401	26 July 2016	31 October 2022
PMB	9773	5415	13 July 2021	31 October 2022
RVD	63,716	34,457	27 March 2014	28 July 2021
SALT	14,151	9908	21 July 2017	22 December 2020
STA	40,256	21,751	7 December 2015	19 April 2021
SUN	87,720	47,733	24 May 2010	31 October 2022
SUT	1715	902	8 February 2017	20 April 2017
UBG	38,917	20,646	26 November 2014	6 November 2020
UFS	31,665	17,152	16 January 2014	30 August 2017
UNV	59,100	33,144	23 April 2015	31 October 2022
UNZ	56,399	30,373	11 July 2014	31 October 2022
UPR	78,792	42,128	19 September 2013	31 October 2022
VAN	24,701	13,234	26 August 2016	10 July 2019

Table 3. Model development stations indicating the mean GHI, DNI and GHI and sizes of training, validation and testing sets.

Station	Mean[1]			Dataset[2]				Cluster Allocation
	GHI [W/m^2]	DNI [W/m^2]	DHI [W/m^2]	Total	Train	Validation	Test	
CSIR	575	599	167	14,991	7,495	3,748	3,748	2
CUT	609	639	159	9,161	4,580	2,290	2,291	2
FRH	544	583	151	12,224	6,112	3,056	3,056	4
GRT	573	624	151	5,788	2,894	1,447	1,447	4
HLO	550	608	138	7,061	3,530	1,765	1,766	1
ILA	589	680	131	2,709	0	0	2,709	1
KZH	533	517	179	8,782	4,391	2,195	2,196	3
KZW	531	511	184	5,945	2,972	1,486	1,487	3
NMU	556	545	165	10,562	5,281	2,640	2,641	4
NUST	614	670	149	15,901	7,950	3,975	3,976	1
MIN	564	573	161	2,761	0	0	2,761	2
RVD	630	729	125	19,624	9,812	4,906	4,906	1
SUN	556	645	133	28,508	14,254	7,127	7,127	1
UBG	591	602	158	12,137	6,068	3,034	3,035	2
UFS	567	654	137	10,257	5,128	2,564	2,565	2
UNV	579	524	197	15,874	7,937	3,968	3,969	2
UNZ	530	528	176	10,055	5,027	2,514	2,514	3
UPR	568	609	163	28,089	14,044	7,022	7,023	2
VAN	597	683	126	7,860	3,930	1,965	1,965	1

[1] Daylight average, [2] Dataset size after quality control as in [40] and $0.175 \leq K_t \leq 0.875$

Preprints.org (www.preprints.org) | NOT PEER-REVIEWED | Posted: 7 March 2024 doi:10.20944/preprints202403.0416.v1

2.2. Comparison Metrics

The comparison metrics are the root mean square error (RMSE), mean absolute error (MAE) and mean bias error (MBE).

$$\begin{aligned} \text{RMSE} &= \sqrt{\sum_{i=1}^{N} \frac{(x_i - \hat{x}_i)^2}{n}}, \\ \text{MAE} &= \frac{1}{n}\sum_{i=1}^{n} |x_i - \hat{x}_i|, \\ \text{MBE} &= \frac{1}{n}\sum_{i=1}^{n} (x_i - \hat{x}_i), \end{aligned} \tag{8}$$

where x_i is the measured value, and $\hat{x}_i$ is the predicted value. A low RMSE and MAE indicate a good model, whereas an MBE should be closer to zero. RMSE indicates the concentration of data around the line of best fit. Therefore, a smaller RMSE is indicative of a more accurate model.

The Pearson correlation coefficient r indicates the correlation between data:

$$r = \frac{\sum (x_i - \bar{x})(y_i - \bar{y})}{\sqrt{\sum (x_i - \bar{x})^2 \sum (y_i - \bar{y})^2}}. \tag{9}$$

In Equation (9), x_i and y_i represent the individual points with index i and $\bar{x}$ and $\bar{y}$ represent the mean of the x and y sample set. An r closer to -1 has a negative correlation, meaning if one variable increases, the other decreases. In contrast, if r is closer to 1, it has a positive correlation, meaning if one variable increases, the other would also [41].

Statistical indicators used for the comparison metrics are the MBE, RMSE and MAE, all expressed as a percentage of the mean measured DNI [26] and R^2. Further comparison metrics are two MAE K_t-intervals: $K_t < 0.60$ and $K_t \geq 0.60$.

The MBE indicates whether a model over or underestimates the DNI, and the RMSE indicates the deviation of the errors. A significant difference between MAE and RMSE indicates a larger variance in the data. Lower RMSE and MAE are ideal, whereas an MBE closer to zero is optimal. The MAE is an unbiased estimator and also evaluates the two K_t intervals. Lower and higher K_t indicate overcast and clear-sky conditions, respectively. Therefore, the two K_t intervals assess the models under varying weather conditions.

2.3. Regression and Fitting

The relationship between two variables is quantified using statistical methods like regression. Regression techniques can be linear, multi-linear and non-linear.

The definition of a linear relationship is

$$y = b_0 + b_1 x, \tag{10}$$

where y is the response, x is the regressor, b_0 is the intercept, and b_0 is the slope. A regression analysis quantifies the strength of a relationship between y and x [41].

The least squares method estimates b_0 and b_1 so that the sum of the squares of the residuals is at a minimum. The residual sum of squares is denoted as SSE and is the sum of squares of the errors about the regression line. Thus, the minimisation of

$$\text{SSE} = \sum_{i=1}^{n} (y_i - \hat{y}_i)^2, \tag{11}$$

where $\hat{y}$ denotes the predicted or fitted value.

 doi:10.20944/preprints202403.0416.v1

The coefficient of determination, R^2, indicates how good the fit of a model is and is a number between zero and one.

$$R^2 = 1 - \frac{\sum (y_i - \hat{y}_i)^2}{(y_i - \bar{y}_i)^2}. \tag{12}$$

A higher R^2-value indicates that the model explains the variation in the response variable around its mean, and the regression model fits the observation better [41].

Polynomial regression is the modelling of a dependent, y, as an n^{th}-degree polynomial of x

$$y = b_o + b_1 x + b_2 x^2 + \cdots + b_r x^2. \tag{13}$$

Exponential regression is where the best fit of an equation is an exponential function, like

$$y = a + bc^x, \tag{14}$$

or

$$y = a + be^{cx}. \tag{15}$$

Multi-linear regression has multiple variables, which is the outcome of a response variable

$$y = \beta_0 + b_1 x_{1i} + b_2 x_{2i} + \cdots + b_k x_{ki}. \tag{16}$$

2.4. Software Development Tools

The model development utilises a combination of data science applications and modelling. The primary tool is the open-source language Python with the anaconda interface [42], and various available libraries [43–45].

2.5. Baseline Models

Three comparative models are used as a baseline to compare the new models. Based on the literature, the DISC and Dirint models performed well for Southern African climates [38,46].

The Dirint [18] and Lee [3] models are also used for comparison because their foundation is similar to the DISC model [17].

Maxwell's DISC quasi-physical approach has three assumptions [3]:

1. The relative air mass AM is the dominant parameter affecting the relationship between K_n and K_t;
2. The physical model used to calculate K_n will provide a physically-based reference from which the changes in K_n can be calculated (see Equation (20) below);
3. Seasonal, annual and climate variations in the relationship between K_n and K_t are fully accounted for by parametric functions in K_t that relate ΔK_n to AM, cloud cover and PW vapour.

AM is defined as [47]

$$AM = \left[\cos\theta_Z + 0.5057 \cdot (96.080 - \theta_Z)^{-1.634}\right]^{-1}. \tag{17}$$

The absolute AM (AM_a) is the pressurised normalisation of AM, expressed as

$$AM_a = \text{AM}\left(\frac{P}{P_o}\right), \tag{18}$$

where P refers to the atmospheric pressure at the test site, and P_o is the atmospheric pressure at sea level.

Preprints.org (www.preprints.org) | NOT PEER-REVIEWED | Posted: 7 March 2024 doi:10.20944/preprints202403.0416.v1

The modelled DNI is determined using Equation (3):

$$DNI = G_{0n} \cdot K_n, \tag{19}$$

where

$$K_n = K_{nc} - \Delta K_n, \tag{20}$$

and

$$\Delta K_n = a_{\text{DISC}} + b_{\text{DISC}} e^{c_{\text{DISC}} \cdot AM}. \tag{21}$$

The clear-sky limit K_{nc} is a polynomial in AM:

$$K_{nc} = 0.866 - 0.122AM + 0.0121AM^2 - 0.00653AM^3 + 0.000014AM^4. \tag{22}$$

Two K_t intervals determine the coefficients $a_{\text{DISC}}, b_{\text{DISC}}$ and c_{DISC}: $K_t \leq 0.60$ and $K_t > 0.60$.
For $K_t \leq 0.60$

$$\begin{aligned} a_{\text{DISC}} &= 0.512 - 1.56K_t + 2.286K_t^2 - 2.222K_t^3, \\ b_{\text{DISC}} &= 0.370 + 0.962K_t^3, \\ c_{\text{DISC}} &= -0.280 + 0.932K_t - 2.048K_t^2. \end{aligned} \tag{23}$$

For $K_t > 0.60$

$$\begin{aligned} a_{\text{DISC}} &= -5.743 + 21.77K_t - 27.49K_t^2 + 11.56K_t^3, \\ b_{\text{DISC}} &= 41.4 - 118.5K_t + 66.05K_t^2 + 31.90K_t^3, \\ c_{\text{DISC}} &= -47.01 + 184.2K_t - 222.0K_t^2 + 73.81K_t^3. \end{aligned} \tag{24}$$

Maxwell's model possesses a different functional form because the quasi-physical approach is applied; therefore, it partially reflects the physics involved in the atmospheric transmission of solar radiation [3]. The a_{DISC}, b_{DISC} and c_{DISC} parameters were fitted based on solar radiation data from Atlanta, Georgia, USA, 1981 [17]. Maxwell adopted the Bird clear-sky model for K_{nc} (see Equation (22)). The parameters a_{DISC}, b_{DISC} and c_{DISC}, as described in Equations (23) and (24), were then fitted based on the dataset.

The DISC model, termed 'quasi-physical', combines a clear-sky model with experimental fits for other sky conditions. The model is a clear-sky irradiance attenuated by a function of K_t. Maxwell derived the empirical regressions from 12 years of recorded radiation data at 70 stations [4,17].

The Dirint model is based on the DISC model and was developed by Perez *et al.* [18]. The goal was to improve the accuracy of the DISC model by Maxwell [17].

The Dirint model uses a clearness index variation parameter K_t':

$$K_t' = \frac{K_t}{1.031e^{-1.4/(0.9+9.4/AM)} + 0.1}. \tag{25}$$

Furthermore, a stability index parameter $\Delta K_t'$:

$$\Delta K_t' = 0.5\left(|K'_{t(i)} - K'_{t(i+1)}| + |K'_{t(i)} - K'_{t(i-1)}|\right), \tag{26}$$

considers the previous $(i-1)$, current (i) and next hourly $(i+1)$ record. When the preceding or hourly record is missing, $\Delta K_t'$ is

$$\Delta K_t' = |K_{t(i)} - K_{t(i\pm1)}|. \tag{27}$$

A low $\Delta K_t'$ is a stable condition, whereas a high $\Delta K_t'$ characterises unstable conditions, which allows the distinction between hazy and partly cloudy conditions. The T_d is an adequate atmospheric PW estimator [18]. The Dirint model's atmospheric PW (W) is estimated using:

$$W = \exp(0.07 \cdot T_d - 0.075). \tag{28}$$

Preprints.org (www.preprints.org) | NOT PEER-REVIEWED | Posted: 7 March 2024 doi:10.20944/preprints202403.0416.v1

The Dirint is a four-dimension conditional model, having the θ_Z, K_t, $\Delta K_t'$ and W. Based on the four-dimensional model, the calculation of hourly DNI is

$$DNI = \frac{I_{0n} \cdot k_b' e^{-1.4/(0.9+9.4/AM)}}{0.87291}. \tag{29}$$

where

$$\begin{aligned} k_b' &= 0 \text{ for } K_t' < 0.2, \\ k_b' &= a_{\text{Dirint}} K_t' + b_{\text{Dirint}}. \end{aligned} \tag{30}$$

Coefficients a_{Dirint} and b_{Dirint} are from a complex lookup table.

Lee *et al.* created a new model for Korea with the same format as Maxwell's DISC model.

$$\begin{aligned} a_{\text{Lee}} &= 0.342 - 0.3782K_t, \\ b_{\text{Lee}} &= 0.5329 + 0.2676K_t - 0.0216k_t^2 + 0.1584K_t^3. \end{aligned} \tag{31}$$

For $K_t \leq 0.5$

$$c_{\text{Lee}} = -0.2117 - 0.0513K_t + 1.2976K_t^2 - 3.3222K_t^3 \tag{32}$$

or $K_t > 0.5$

$$c_{\text{Lee}} = 0.7221 - 10.2801K_t + 30.3285K_t^2 - 27.9766K_t^3. \tag{33}$$

The evaluation consists of comparing the localised, clustered and regional models against the three baseline models: DISC, Dirint and Lee. The DISC and Dirint models were selected based on their performance in estimating DNI for Southern African climates. The Lee and Dirint models have foundational similarities to the DISC model. These models consider whether the newly developed decomposition model improves the accuracy of hourly DNI estimations for Southern Africa. The accuracy evaluation uses the comparison metrics discussed in the next section.

2.6. Decomposition Model Development Methodology

The methodology builds on the DISC model. The DISC model stands out as one of the better-performing models for estimating DNI for South Africa [38]. Its simplicity is evident in its lack of need for a complex four-dimensional lookup table, unlike the Dirint model.

The original DISC model uses Equation (21), an exponential function. However, the regression model for an exponential function, as discussed in Section 2.3, showed difficulty in finding optimal a, b and c coefficients in all cases. Instead, a second-order polynomial function of AM

$$\Delta K_n = a + b \cdot AM + c \cdot AM^2 \tag{34}$$

is a suitable substitute with similar regression results.

The training set then fits a, b and c for intervals $K_t \leq 0.60$ and $K_t > 0.60$:

$$\begin{aligned} a &= a_0 + a_1 K_t + a_2 K_t^2 + a_3 K_t^3, \\ b &= b_0 + b_1 K_t + b_2 K_t^2 + b_3 K_t^3, \\ c &= c_0 + c_1 K_t + c_2 K_t^2 + c_3 K_t^3, \end{aligned} \tag{35}$$

and the validation and testing sets evaluate the model's accuracy.

Each model development undergoes the following initial processing steps:

1. Empirical formulae estimate θ_Z, AM, pressure, I_{0n}, K_t and K_n. From this, the assessment of available models aids in developing a new model;
2. Data is split into intervals of 0.05 K_t, starting from 0.175 to 0.875;
3. ΔK_n is then modelled as Equation (34);

Preprints.org (www.preprints.org) | NOT PEER-REVIEWED | Posted: 7 March 2024 doi:10.20944/preprints202403.0416.v1

4. The interval or intervals are then fitted against the function to determine Equation (34) to determine the a, b and c coefficients using a least squares regression analysis;
5. From the K_t-interval function, the a_0-a_3, b_0-b_3 and c_0-c_3 coefficients are fitted to a polynomial of Equation (35) with regards to K_t;
6. These equations can be used to determine ΔK_n and K_n, which, in turn, calculates the DNI (see Equations (19) and (20)).

For each SAURAN station, a localised decomposition model is developed. A clustered decomposition model describes an area with similar irradiance patterns using the clustered areas discussed in [40]. Farmer and Rix first presented a two-cluster correlation map using the SAURAN database [48] and, by using this approach, this study formulated four clusters instead of two in Southern Africa, as shown in Figure 3a.

Figure 3a shows the clusters' geographical location, and Figure 3b shows the penetration levels of GHI. Table 4 shows the different clusters' training sets' mean GHI, DNI and DHI.

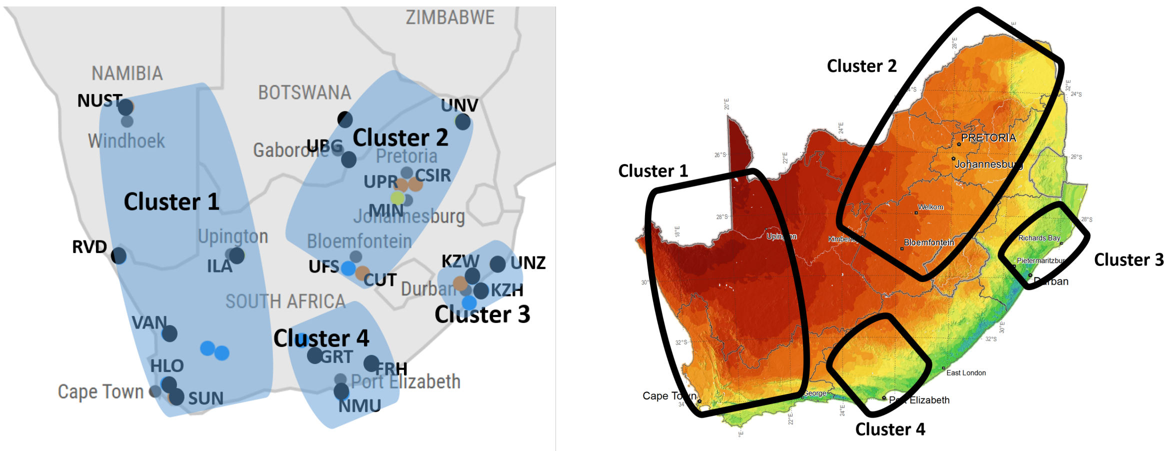

a SAURAN [39]. **b** GHI across South Africa [49].

Figure 3. Clusters within the Southern African context.

Table 4. Clusters mean irradiances.

	Mean[4]		
	GHI $[W/m^2]$	**DNI** $[W/m^2]$	**DHI** $[W/m^2]$
Cluster 1	592	669	135
Cluster 2	583	604	165
Cluster 3	534	523	178
Cluster 4	557	579	158

[4] Mean values of training set

Cluster 1 receives the most GHI and DNI, and Cluster 3 receives the least, as evident from Figure fig:Clustersb. The different climates are also evident in these clusters: Cluster 3 is more humid and receives, on average, more DHI than Cluster 1.

Figure 4 shows how the cluster data is combined. Each cluster and the regional (Southern African) model are combined with even distributions of datasets to avoid introducing a bias, as some stations are over-represented in the original data set. Some stations, such as the SUN, UPR and RVD stations, have considerably more data available as they are either older stations or have not been closed down.

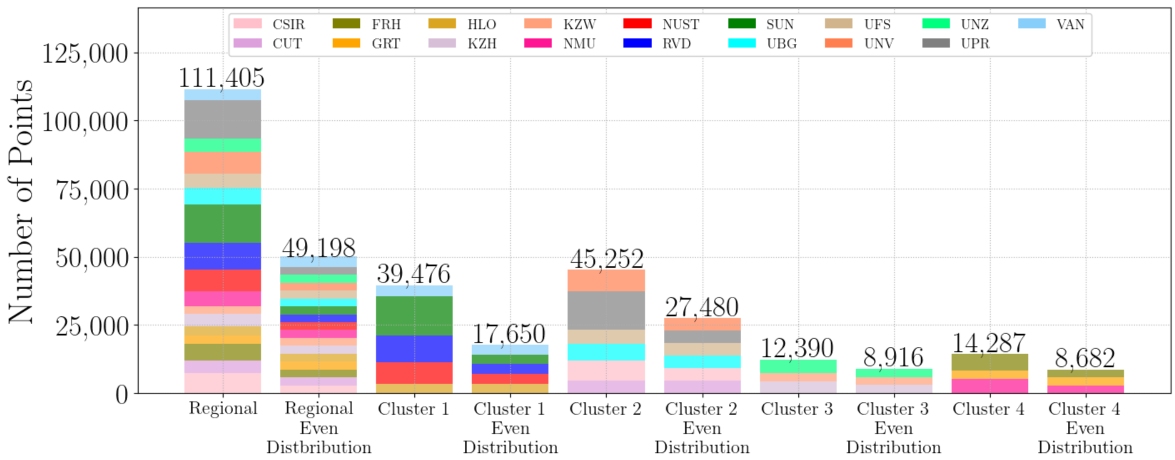

Figure 4. Distribution of data within clusters.

The different stations have varying climates, and therefore, a larger representation of one station will result in a biased model towards that station. The advantage of the even distribution is that every station is sufficiently represented and will not cause a model bias, but this reduces the amount of available data.

Cluster 2's stations have higher elevation and summer humidity due to its warm, rainy summers and dry, cold winters. The expected annual irradiance levels are lower, as seen in Figure 3b. The stations have higher humidity because of their location and higher DHI levels.

The two stations in Cluster 2, UPR and CSIR, are expected to have more diffuse particles due to the higher air pollution levels and, therefore, higher DHI levels. Cluster 2 has a large bias of the data from Pretoria, South Africa, from the CSIR and UPR datasets.

Cluster 4 has lower annual irradiance levels, as seen in Figure 3b, and FRH and NMU are closer to the coastline, whereas GRT is inland.

3. Development of New Decomposition Models

This section discusses the newly developed a, b and c coefficients of Equation (34).

The section consists of three subsections:

1. The localised decomposition models, developed using the training dataset of the SAURAN station;
2. The clustered decomposition models, which are modelled on the training data of all the stations within the cluster, as discussed in Figure 4;
3. And the regional model is modelled on all the stations' training data (Table 3).

3.1. Localised Decomposition Models

The localised decomposition model equations for the a, b and c coefficients are presented in Appendix A.

3.2. Cluster Decomposition Models

Figures 5–8 show the different corresponding clusters' model coefficients.

3.2.1. Cluster 1

Cluster 1 comprises the HLO, NUST, RVD, SUN and VAN datasets, as shown in Figures 3a and 4.

Figure 5 shows the Cluster 1 and five stations' a, b and c coefficients. The discussion of the different stations is in Appendix A under Subsections A.5 (HLO), A.11 (NUST), A.12 (RVD), A.13 (SUN) and A.19 (VAN).

The RVD model is the only model showing difficulty fitting the coefficients with K_t. Table 3 indicates that the RVD station has the highest mean DNI and GHI, with the lowest DHI measurements, compared to the rest of Cluster 1's stations.

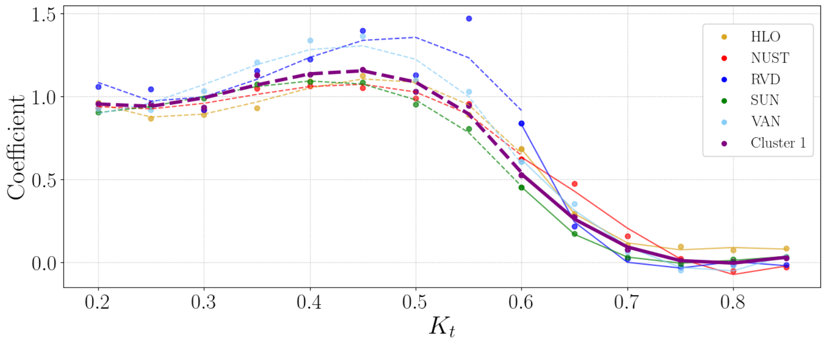

a *a* coefficient.

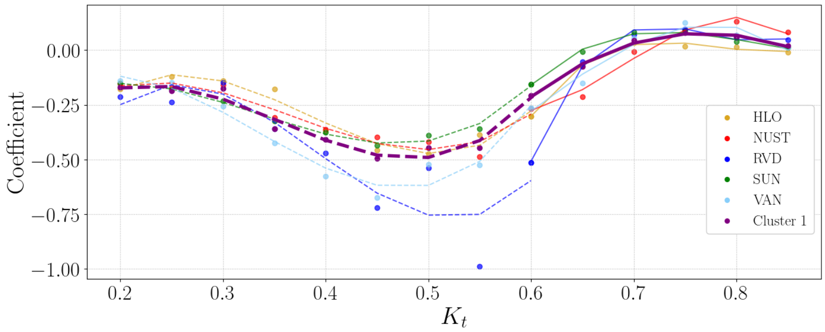

b *b* coefficient.

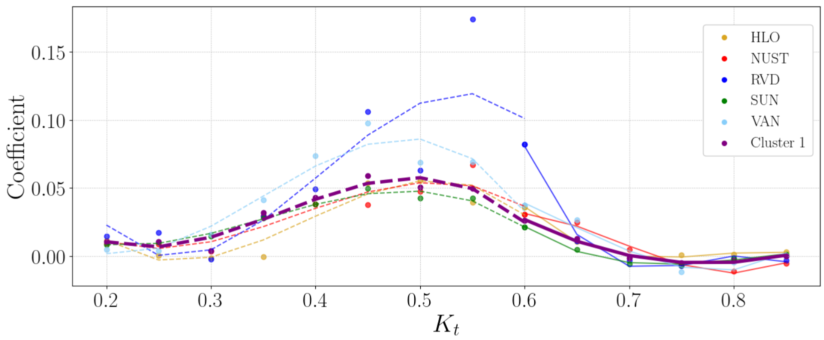

c *c* coefficient.

Figure 5. Cluster 1 coefficients in $\Delta K_n = a + b \cdot AM + c \cdot AM^2$.

The coefficients for Cluster 1 are

$$a = \begin{cases} 2.4134 - 15.428K_t + 50.7433K_t^2 - 50.3864K_t^3 \text{ for } K_t < 0.60, \\ 18.4363 - 61.7241K_t + 67.5365K_t^2 - 23.9963K_t^3 \text{ for } K_t \geq 0.60 \end{cases}$$
$$b = \begin{cases} -1.4538 + 13.4628K_t - 43.4278K_t^2 + 40.7081K_t^3 \text{ for } K_t < 0.60, \\ -7.7071 + 23.0993K_t - 20.5561K_t^2 + 4.7883K_t^3 \text{ for } K_t \geq 0.60 \end{cases} \quad (36)$$
$$c = \begin{cases} 0.2232 - 2.1593K_t + 6.6964K_t^2 - 6.0805K_t^3 \text{ for } K_t < 0.60, \\ 0.7064 - 1.9679K_t + 1.5214K_t^2 - 0.2153K_t^3 \text{ for } K_t \geq 0.60 \end{cases}$$

3.2.2. Cluster 2

Cluster 2 consists of the CSIR, CUT, UBG, UFS, UPR, and UNV datasets. Figure 6 shows the Cluster 2 and six stations' a, b and c coefficients.

The discussion of the different stations are in Appendix A under Subsections A.1 (CSIR), A.2 (CUT), A.14 (UBG), A.15 (UFS), A.18 (UPR) and A.16 (UNV). The UFS have the greatest deviation from the Cluster 2 fit.

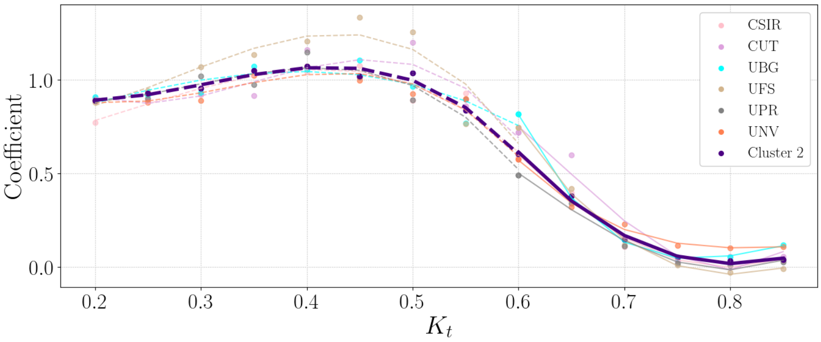

a a coefficient.

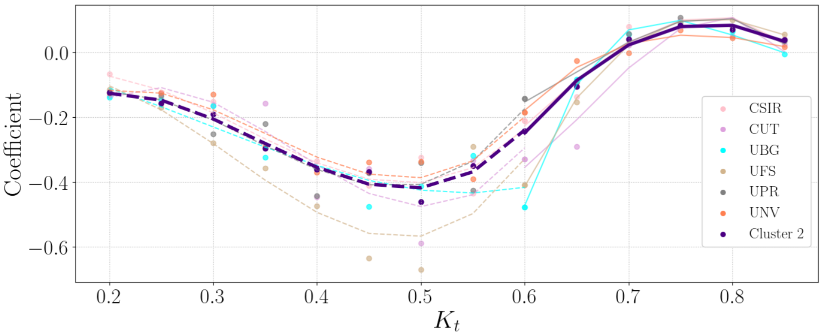

b b coefficient.

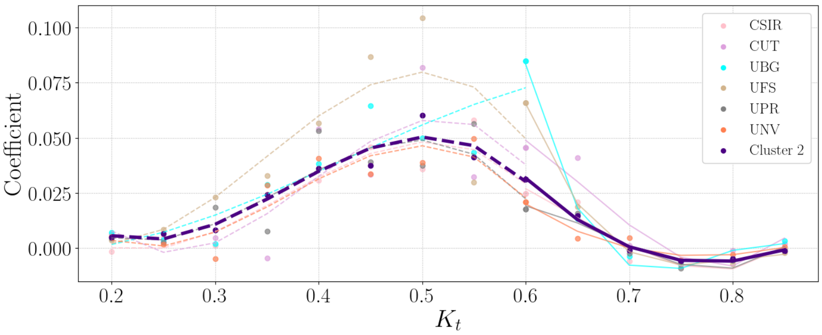

c c coefficient.

Figure 6. Cluster 2 coefficients in $\Delta K_n = a + b \cdot AM + c \cdot AM^2$.

The coefficients for Cluster 2 are

$$a = \begin{cases} 1.4234 - 6.6647K_t + 25.5673K_t^2 - 27.8939K_t^3 \text{ for } K_t < 0.60, \\ 10.5939 - 28.4856K_t + 21.7611K_t^2 - 3.348K_t^3 \text{ for } K_t \geq 0.60. \end{cases}$$
$$b = \begin{cases} -0.8033 + 7.723K_t - 26.9074K_t^2 + 25.9995K_t^3 \text{ for } K_t < 0.60, \\ -6.1286 + 15.6674K_t - 9.4832K_t^2 - 0.4949K_t^3 \text{ for } K_t \geq 0.60. \end{cases} \quad (37)$$
$$c = \begin{cases} 0.1604 - 1.5968K_t + 5.0219K_t^2 - 4.537K_t^3 \text{ for } K_t < 0.60, \\ 0.8966 - 2.6121K_t + 2.2392K_t^2 - 0.4802K_t^3 \text{ for } K_t \geq 0.60. \end{cases}$$

3.2.3. Cluster 3

Cluster 3 consists of the KZH, KZW and UNZ datasets. Figure 7 shows the Cluster 3 and three stations' a, b and c coefficients.

The discussion of the different stations is in Appendix A under Subsections A.7 (KZH), A.8 (KZW) and A.17 (UNZ). The three models fit quite well and are similar to Cluster 3.

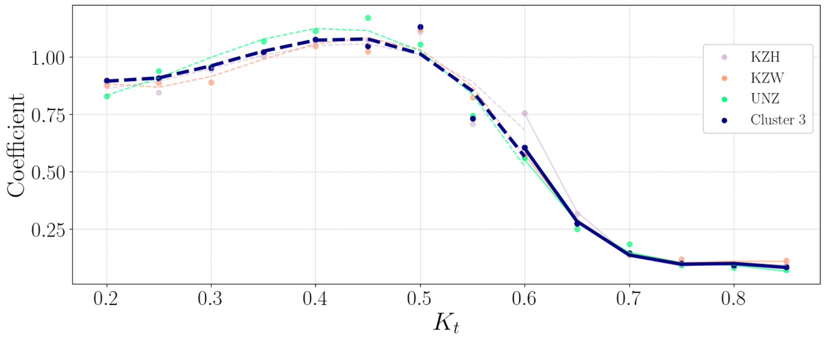

a a coefficient.

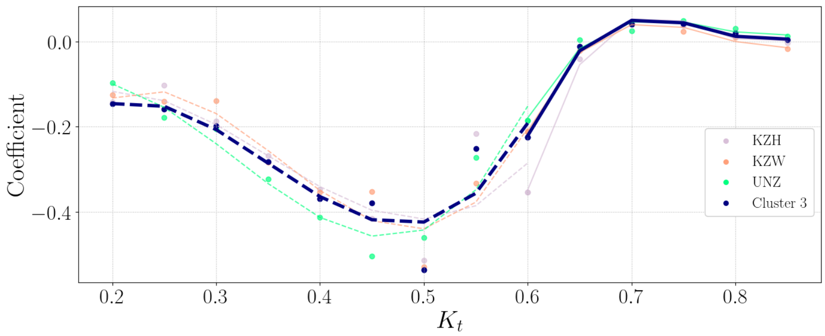

b b coefficient.

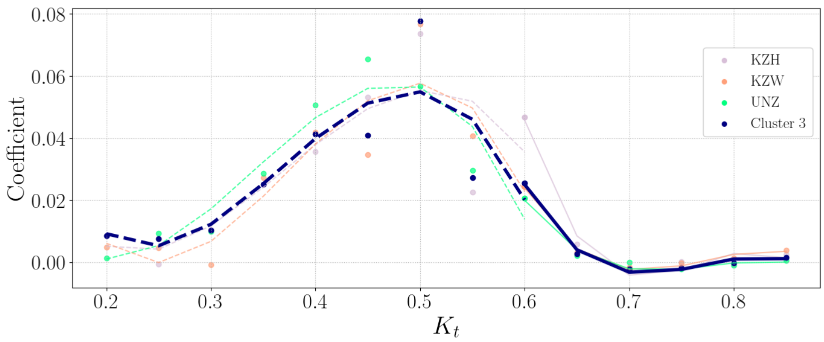

c c coefficient.

Figure 7. Cluster 3 coefficients in $\Delta K_n = a + b \cdot AM + c \cdot AM^2$.

The coefficients for Cluster 3 are

$$a = \begin{cases} 1.7678 - 9.8995K_t + 34.9076K_t^2 - 36.2495K_t^3 \text{ for } K_t < 0.60, \\ 41.1735 - 157.5062K_t + 201.1335K_t^2 - 85.5391K_t^3 \text{ for } K_t \geq 0.60. \end{cases}$$
$$b = \begin{cases} -1.0914 + 10.2302K_t - 33.9924K_t^2 + 32.4023K_t^3 \text{ for } K_t < 0.60, \\ -31.151 + 121.964K_t - 158.1413K_t^2 + 67.9737K_t^3 \text{ for } K_t \geq 0.60. \end{cases} \tag{38}$$
$$c = \begin{cases} 0.2256 - 2.1961K_t + 6.8092K_t^2 - 6.1997K_t^3 \text{ for } K_t < 0.60, \\ 3.4215 - 13.4513K_t + 17.5277K_t^2 - 7.5726K_t^3 \text{ for } K_t \geq 0.60. \end{cases}$$

3.2.4. Cluster 4

Cluster 4 consists of the NMU, FRH and GRT datasets. Figure 8 shows the Cluster 4 and three stations' a, b and c coefficients.

The discussion of the different stations is in Appendix Avvvv under Subsections A.10 (NMU), A.3 (FRH) and A.4 (GRT). The GRT station's c-coefficient does show difficulty in a fit determination.

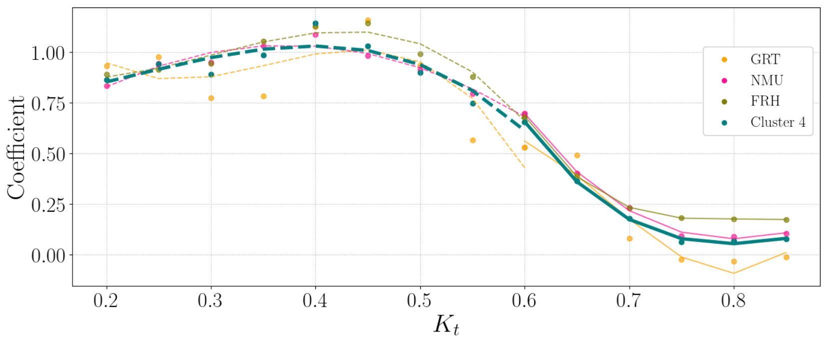

a a coefficient.

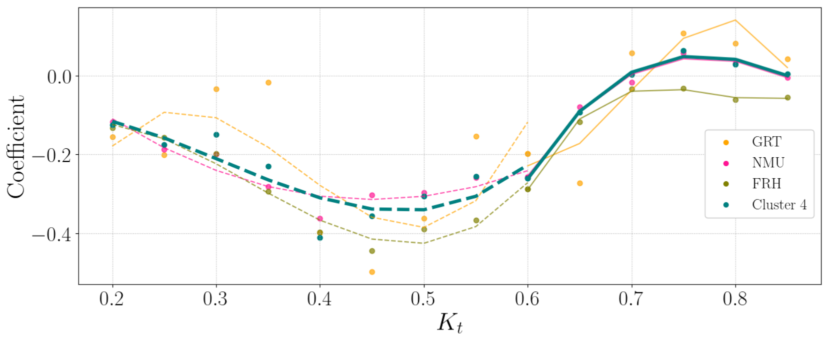

b b coefficient.

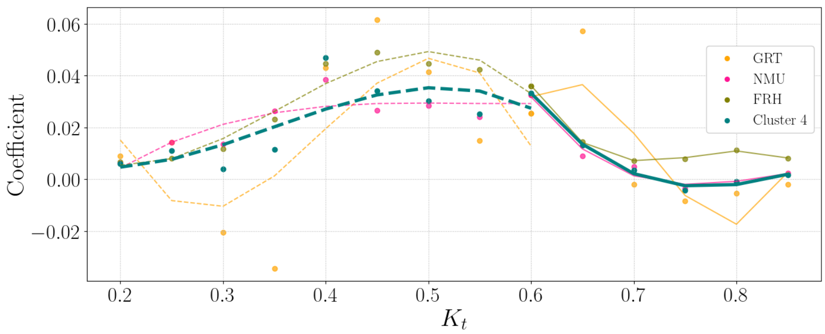

c c coefficient.

Figure 8. Cluster 4 coefficients in $\Delta K_n = a + b \cdot AM + c \cdot AM^2$.

Preprints.org (www.preprints.org) | NOT PEER-REVIEWED | Posted: 7 March 2024 doi:10.20944/preprints202403.0416.v1

The coefficients for Cluster 4 are

$$
\begin{aligned}
a &= \begin{cases} 0.7671 - 0.9387K_t + 9.7073K_t^2 - 14.2827K_t^3 \text{ for } K_t < 0.60, \\ 20.0495 - 67.0086K_t + 73.6919K_t^2 - 26.4669K_t^3 \text{ for } K_t \geq 0.60. \end{cases} \\
b &= \begin{cases} -0.2382 + 2.3908K_t - 11.3676K_t^2 + 12.3585K_t^3 \text{ for } K_t < 0.60, \\ -12.5095 + 42.6536K_t - 47.1486K_t^2 + 16.8022K_t^3 \text{ for } K_t \geq 0.60. \end{cases} \\
c &= \begin{cases} 0.0451 - 0.5012K_t + 1.8485K_t^2 - 1.7706K_t^3 \text{ for } K_t < 0.60, \\ 1.4976 - 5.1597K_t + 5.8075K_t^2 - 2.1264K_t^3 \text{ for } K_t \geq 0.60. \end{cases}
\end{aligned} \tag{39}
$$

3.3. Regional Decomposition Model

The regional (Southern African) decomposition model data is an even distribution of the SAURAN stations regarding the number of data points used per station. Multiple climates, different elevations and pollution levels are represented within the dataset, leading to a better decomposition model for Southern Africa and a regional application.

Figure 9 shows the coefficients a, b and c of the regional model and the four clusters.

The coefficients for the regional model are

$$
\begin{aligned}
a &= \begin{cases} 1.2893 - 5.2531K_t + 21.5081K_t^2 - 24.5156K_t^3 \text{ for } K_t < 0.60, \\ 19.0295 - 63.9357K_t + 70.7485K_t^2 - 25.6524K_t^3 \text{ for } K_t \geq 0.60. \end{cases} \\
b &= \begin{cases} -0.6327 + 5.891K_t - 21.4431K_t^2 + 21.2593K_t^3 \text{ for } K_t < 0.60, \\ -11.7813 + 39.923K_t - 43.6596K_t^2 + 15.3252K_t^3 \text{ for } K_t \geq 0.60. \end{cases} \\
c &= \begin{cases} 0.1118 - 1.1105K_t + 3.6089K_t^2 - 3.3222K_t^3 \text{ for } K_t < 0.60, \\ 1.49 - 5.2009K_t + 5.9381K_t^2 - 2.2137K_t^3 \text{ for } K_t \geq 0.60. \end{cases}
\end{aligned} \tag{40}
$$

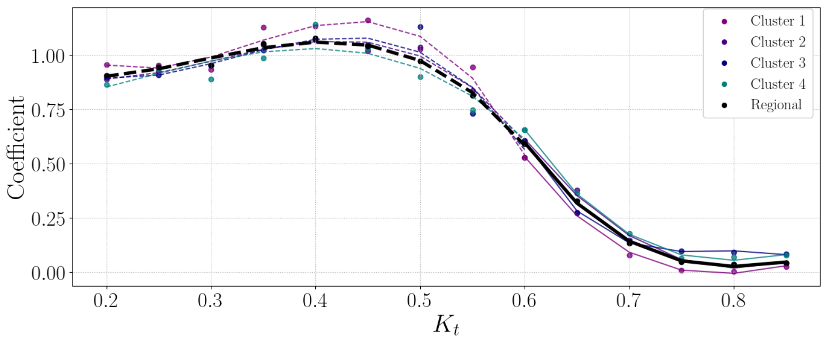

a a coefficient.

Figure 9. *Cont.*

 doi:10.20944/preprints202403.0416.v1

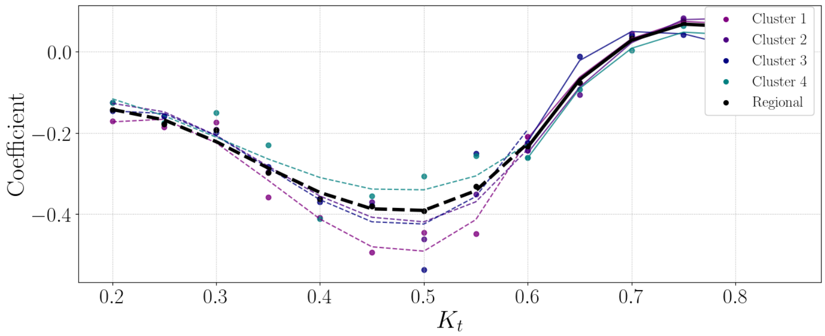

b *b* coefficient.

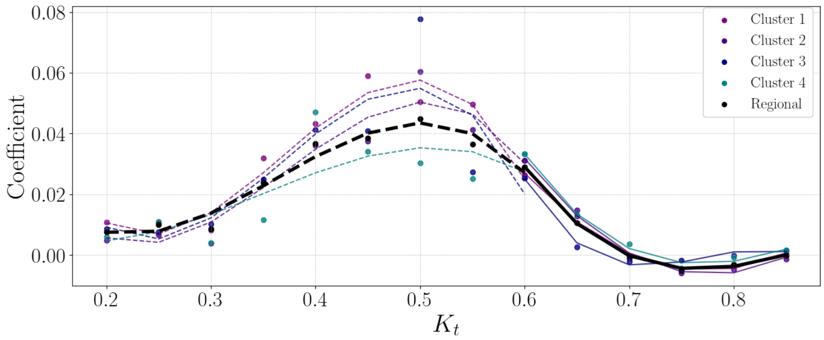

c *c* coefficient.

Figure 9. Regional model coefficients in $\Delta K_n = a + b \cdot AM + c \cdot AM^2$.

4. Results

Each station is discussed individually by assessing the dataset's comparison metrics: the R^2-value, MBE, RMSE and MAE, and the MAE of two K_t-intervals. The results compare the localised, clustered and regional (Southern African) models to the three baseline models, DISC, Dirint and Lee. The tables visualise the results for each station using red and green, with green denoting lower error and red denoting higher error.

Table 3 discusses the validation data. In the previous section, the localised, clustered, and regional models were empirically determined. Appendix A expands on the equations for the localised models.

Sections 3.2 and 3.3 discussed the clustered and regional models. The test data also introduces two unknown datasets, the ILA and MIN datasets. These datasets assess the models with new data for the developed models. ILA and MIN have no localised model, but geographically, they fall within a cluster: ILA falls under Cluster 1 and MIN under Cluster 2.

4.1. Testing and Validation Results

4.1.1. CSIR

Section A.1 shows the decomposition model equations for the CSIR station. Table 5 shows the results of the CSIR station. The results show that the localised, Cluster 2 and regional models outperform the baseline models in all metrics. The localised model significantly improves for lower K_t, reducing the MAE from around 60% to 36%.

The test results of the CSIR dataset are presented in Figure A1. As seen in the figure, the localised, cluster, and regional models outperform the baseline models, consistent with the validation results of the previous section in Table 5.

Preprints.org (www.preprints.org) | NOT PEER-REVIEWED | Posted: 7 March 2024 doi:10.20944/preprints202403.0416.v1

Table 5. Hourly validation results of decomposition model development for CSIR.

Model	Entire Dataset				$K_t < 0.60$	$K_t \geq 0.60$
	R^2	MBE [%]	RMSE [%]	MAE [%]	MAE [%]	MAE [%]
DISC	0.52	-10.6	39.7	32.5	60.7	25.2
Dirint	0.59	-20.2	37.8	30.3	61.6	22.3
Lee	0.62	6.49	31.0	25.3	56.9	17.2
CSIR	0.72	1.19	25.8	19.5	36.2	15.3
Cluster 2	0.72	1.59	25.9	19.4	35.7	15.3
Regional	0.72	4.32	26.3	19.6	36.2	15.4

4.1.2. CUT

Section A.2 shows the decomposition model equations for the CUT station. Table 6 shows the CUT station results. The localised Cluster 2 and regional model significantly improve the comparison metrics over the three baseline models. The Lee model has a similar MBE to the regional model (±0.7) and has a higher K_t-metric similar to Cluster 2. However, the Lee RMSE and MAE still do not outperform the new models.

Figure A2 presents the test results of the CUT dataset, where the localised, cluster and regional models outperform the baseline models. The test results are consistent with the validation results presented in Table 6.

Table 6. Hourly validation results of decomposition model development for CUT.

Model	Entire Dataset				$K_t < 0.60$	$K_t \geq 0.60$
	R^2	MBE [%]	RMSE [%]	MAE [%]	MAE [%]	MAE [%]
DISC	0.55	-15.7	38.0	31.2	61.0	23.9
Dirint	0.6	-23.4	38.6	31.8	62.3	24.4
Lee	0.6	0.7	30.9	24.9	56.5	17.2
CUT	0.71	-1.8	26.0	20.1	33.7	16.8
Cluster 2	0.7	-1.6	26.2	20.5	34.6	17.1
Regional	0.7	0.66	26.3	20.3	34.7	16.7

4.1.3. FRH

Section A.3 shows the decomposition model equations for the FRH station. Table 7 shows the results of the FRH station. The localised model outperforms the baseline models by improving R^2 and MBE and reducing MAE and RSME. The Lee model shows the lowest MAE for higher K_t-values; however, it does show an overestimation for DNI with a higher MBE. For most metrics, the localised, Cluster 4 and regional model outperforms the baseline models.

Figure A3 presents the test results of the FRH dataset. The localised Cluster 2 and regional models outperform the baselines, but no significant difference exists between the new three models. The test results presented in Figure A3 correspond with the validation results in Table 7.

Table 7. Hourly validation results of decomposition model development for FRH.

Model	Entire Dataset				$K_t < 0.60$	$K_t \geq 0.60$
	R^2	MBE [%]	RMSE [%]	MAE [%]	MAE [%]	MAE [%]
DISC	0.51	-5.49	41.8	31.8	60.9	24.0
Dirint	0.52	-15.9	42.0	33.5	63.2	25.6
Lee	0.51	6.71	39.7	29.7	64.1	20.6
FRH	0.58	-0.44	36.0	26.8	44.6	22.1
Cluster 4	0.58	-0.28	36.0	26.4	45.5	21.4
Regional	0.57	2.63	36.2	26.1	44.5	21.2

Preprints.org (www.preprints.org) | NOT PEER-REVIEWED | Posted: 7 March 2024 doi:10.20944/preprints202403.0416.v1

4.1.4. GRT

Section A.4 shows the decomposition model equations for the GRT station. Table 8 shows the GRT station results. The localised model does show improvement over the DISC and Dirint model but does not significantly outperform the Lee model. The Lee model has a higher R^2, lower MBE AND RMSE, whereas the localised model has a lower MAE for the entire dataset and the two K_t intervals. The Cluster 4 and regional models perform better than the DISC and Dirint models but do not significantly outperform all the baseline models.

Figure A4 shows the test results of the GRT dataset. The results correspond with the validation results in Table 8. The localised, Cluster 4 and regional model does outperform the DISC and Dirint model but only marginally outperforms the Lee model.

Table 8. Hourly validation results of decomposition model development for GRT.

Model	**Entire Dataset**				$\mathbf{K_t < 0.60}$	$\mathbf{K_t \geq 0.60}$
	$\mathbf{R^2}$	**MBE [%]**	**RMSE [%]**	**MAE [%]**	**MAE [%]**	**MAE [%]**
DISC	0.62	-13.9	36.1	28.3	59.1	20.0
Dirint	0.67	-22.8	37.5	30.4	60.4	22.3
Lee	0.67	-0.89	29.4	24.2	59.2	14.8
GRT	0.65	-1.99	32.3	21.0	47.1	13.9
Cluster 4	0.73	-7.43	27.6	21.5	42.9	15.7
Regional	0.71	-4.75	28.0	20.9	42.2	15.2

4.1.5. HLO

Section A.5 shows the decomposition model equations for the HLO station. Table 9 shows the HLO station results. The localised model performs better than the baseline models and improves all comparison metrics.

Figure A5 shows the test results of the HLO dataset. The validation results in Table 9 and the test results correspond well, indicating that the localised Cluster 1 and regional models outperform the baseline models.

Table 9. Hourly validation results of decomposition model development for HLO.

Model	**Entire Dataset**				$\mathbf{K_t < 0.60}$	$\mathbf{K_t \geq 0.60}$
	$\mathbf{R^2}$	**MBE [%]**	**RMSE [%]**	**MAE [%]**	**MAE [%]**	**MAE [%]**
DISC	0.63	-7.95	34.6	27.1	58.7	18.7
Dirint	0.67	-18.4	34.7	27.0	60.5	18.2
Lee	0.67	2.31	29.1	23.3	59.2	13.9
HLO	0.75	-1.16	25.2	18.9	41.3	13.0
Cluster 1	0.75	2.44	25.3	18.8	40.8	13.0
Regional	0.75	-3.69	25.3	19.7	42.3	13.7

4.1.6. ILA

Figure A6 presents the test results of the ILA dataset. The ILA dataset has no localised decomposition model; therefore, the testing only assesses the Cluster 1 and regional models. The results show that the Cluster 1 and regional models outperform the baseline models. The results highlight the substitution of using a Cluster model when no localised model is available, subject to the geographical location within the Cluster area.

4.1.7. KZH

Section A.7 shows the decomposition model equations for the KZH station. Table 10 shows the results of the KZH station. The localised, Cluster 3 and regional models all show significant

Preprints.org (www.preprints.org) | NOT PEER-REVIEWED | Posted: 7 March 2024 doi:10.20944/preprints202403.0416.v1

improvements in reducing the error over the baseline models. The DISC has a lower MBE than the regional model.

Figure A7 shows the test results of the KZH dataset. The localised, Cluster 3 and regional models all outperform the baseline models. The regional model does not outperform Cluster 3 or the localised model significantly.

Table 10. Hourly validation results of decomposition model development for KZH.

Model	Entire Dataset				$K_t < 0.60$	$K_t \geq 0.60$
	R^2	MBE [%]	RMSE [%]	MAE [%]	MAE [%]	MAE [%]
DISC	0.63	-2.15	38.1	30.4	59.3	21.9
Dirint	0.67	-12.7	35.3	28.1	61.0	18.5
Lee	0.67	13.4	35.5	28.6	67.2	17.3
KZH	0.75	-0.29	28.5	21.7	44.5	15.0
Cluster 3	0.75	1.3	28.5	21.7	44.5	15.0
Regional	0.75	4.95	29.0	21.7	45.0	14.9

4.1.8. KZW

Section A.8 shows the decomposition model equations for the KZW station. Table 11 shows the results of the KZW station. The localised, clustered, and regional models show improvement over the baseline models with metrics that assess the entire data set.

Figure A8 shows the test results of the KZW dataset. The validation and testing results from Table 11 correspond.

Table 11. Hourly validation results of decomposition model development for KZW.

Model	Entire Dataset				$K_t < 0.60$	$K_t \geq 0.60$
	R^2	MBE [%]	RMSE [%]	MAE [%]	MAE [%]	MAE [%]
DISC	0.63	-4.26	39.7	31.5	57.1	23.5
Dirint	0.68	-14.8	37.0	28.8	58.5	19.6
Lee	0.67	13.6	36.5	29.9	67.6	18.2
KZW	0.76	1.47	28.9	22.2	43.0	15.7
Cluster 3	0.76	0.58	28.9	22.3	43.2	15.8
Regional	0.75	3.83	29.8	22.5	43.8	15.8

MIN

The test results of the MIN dataset are presented in Figure A9. MIN has no localised decomposition model and falls geographically under Cluster 2. The cluster model and localised model show improvement over the baseline models. Much like the ILA dataset, the MIN dataset demonstrates how the clustered and regional models can serve as alternatives to enhance DNI estimations in Southern Africa.

Ň Section A.10 shows the decomposition model equations for the NMU station. Table 12 shows the NMU station results. The localised, Cluster 4 and regional models show significant improvement in reducing the errors from the baseline models. Based on the higher MBE, the Cluster 4 and regional models overestimate the DNI more than the DISC and Dirint models.

The test results of the NMU dataset are presented in Figure A10. Localised and cluster models outperform baseline models, consistent with the results in Table 12.

Table 12. Hourly validation results of decomposition model development for NMU.

Model	Entire Dataset				$K_t < 0.60$	$K_t \geq 0.60$
	R^2	MBE [%]	RMSE [%]	MAE [%]	MAE [%]	MAE [%]
DISC	0.59	8.72	40.0	29.6	57.7	24.1
Dirint	0.61	-4.49	35.8	26.7	59.9	20.3
Lee	0.61	18.3	39.7	29.3	72.1	21.0
NMU	0.67	0.78	32.5	23.6	49.6	18.5
Cluster 4	0.67	6.98	33.2	22.9	49.7	17.7
Regional	0.66	9.8	34.0	23.2	51.5	17.7

4.1.9. NUST

Section A.11 shows the decomposition model equations for the NUST station. Table 13 shows the results of the NUST station. The localised model shows superior performance over the baseline models, as well as the clustered and regional models. The metrics of the clustered model compared to the baselines indicate that the regional model slightly overestimates the DNI compared to the lowest baseline model (Lee), which slightly underestimates the DNI.

The test results of the NUST dataset are presented in Figure A11. Localised, clustered, and regional models outperform the baseline models, consistent with the validation results presented in Table 13. The regional model shows marginal underperformance compared to the localised and Cluster 1 model, but not significant enough to warrant it as unusable.

Table 13. Hourly validation results of decomposition model development for NUST.

Model	Entire Dataset				$K_t < 0.60$	$K_t \geq 0.60$
	R^2	MBE [%]	RMSE [%]	MAE [%]	MAE [%]	MAE [%]
DISC	0.54	-20.9	39.2	32.6	64.2	24.9
Dirint	0.6	-28.0	40.4	34.0	65.0	26.5
Lee	0.61	-3.36	28.7	23.7	54.3	16.3
NUST	0.74	-0.42	23.0	17.7	29.1	14.9
Cluster 1	0.73	3.11	23.9	17.7	28.2	15.1
Regional	0.72	-2.68	23.8	19.0	31.7	15.9

4.1.10. RVD

Section A.12 shows the decomposition model equations for the RVD station. Table 14 shows the RVD station results. The localised, clustered, and regional models outperform the baseline models. The Lee model performs better than the regional model but does not outperform the localised and cluster models. The RVD station receives more irradiance on average than other stations in the SAURAN database.

Figure A12 shows the test results of the RVD dataset. The results indicate that the localised, cluster and regional models outperform the baseline models, which is consistent with the validation results of the previous section in Table 14. The localised model's RMSE is higher than the Lee model; however, the localised model does best in reducing the error for the other metrics. Though the regional model outperforms the baseline models, it does show the worst performance of the three newly developed models for RVD.

Preprints.org (www.preprints.org) | NOT PEER-REVIEWED | Posted: 7 March 2024 doi:10.20944/preprints202403.0416.v1

Table 14. Hourly validation results of decomposition model development for RVD.

Model	Entire Dataset				$K_t < 0.60$	$K_t \geq 0.60$
	R^2	MBE [%]	RMSE [%]	MAE [%]	MAE [%]	MAE [%]
DISC	0.61	-12.2	29.8	23.1	59.7	16.2
Dirint	0.65	-21.5	32.1	26.4	62.6	19.5
Lee	0.65	-5.21	23.8	18.5	53.3	11.9
RVD	0.76	-0.58	19.0	13.1	30.5	9.7
Cluster 1	0.77	-3.15	18.7	14.3	32.7	10.8
Regional	0.76	-8.64	20.8	17.0	36.4	13.4

4.1.11. SUN

Section A.13 shows the decomposition model equations for the SUN station. Table 15 shows the SUN station results. The localised model outperforms the baseline models by improving R^2 and reducing the MBE, RMSE and MAE. The Cluster 1 and regional models show a slightly worse MBE than the Lee baseline model but otherwise outperform the baseline models. The Lee model also predicts higher K_t points with a lower MAE than the regional model; however, the other metrics indicate that the regional model shows better results overall.

Figure A13 shows the test results of the SUN dataset. The results indicate that the localised, cluster and regional models outperform the baseline models, which is consistent with the testing results of the previous section in Table 15. As with the validation results, the regional model is the worst-performing new model but still outperforms the baseline models.

Table 15. Hourly validation results of decomposition model development for SUN.

Model	Entire Dataset				$K_t < 0.60$	$K_t \geq 0.60$
	R^2	MBE [%]	RMSE [%]	MAE [%]	MAE [%]	MAE [%]
DISC	0.59	-11.1	34.9	27.2	59.8	19.3
Dirint	0.65	-21.5	35.9	28.9	61.2	21.0
Lee	0.65	-2.16	28.2	22.4	55.4	14.4
SUN	0.75	-0.71	23.9	17.8	38.8	12.7
Cluster 1	0.75	-1.9	24.0	18.0	38.1	13.1
Regional	0.75	-7.81	25.3	20.2	40.5	15.3

4.1.12. UBG

Section A.14 shows the decomposition model equations for the UBG station. Table 16 shows the UBG station results. The localised, clustered and regional models all outperform the baseline models. The Lee model has a lower MBE than the Cluster 1 and regional models. The Lee model also has a lower MAE for $K_t \geq 0.60$; however, the other metrics indicate that the model does not improve the R^2, RMSE, overall MAE and $K_t < 0.60$ MAE.

Table 16. Hourly validation results of decomposition model development for UBG.

Model	Entire Dataset				$K_t < 0.60$	$K_t \geq 0.60$
	R^2	MBE [%]	RMSE [%]	MAE [%]	MAE [%]	MAE [%]
DISC	0.36	-11.7	47.2	37.4	66.5	30.4
Dirint	0.41	-20.4	45.9	36.9	66.8	29.6
Lee	0.44	5.4	39.8	28.5	58.9	21.2
UBG	0.46	-0.53	38.7	25.0	40.5	21.3
Cluster 2	0.51	0.4	36.1	24.5	40.8	20.5
Regional	0.51	3.07	36.4	24.1	41.3	19.9

Preprints.org (www.preprints.org) | NOT PEER-REVIEWED | Posted: 7 March 2024 doi:10.20944/preprints202403.0416.v1

Figure A14 shows the test results of the UBG dataset. The test results show that the localised, Cluster 1 and regional models outperform the baseline models. The Lee model has a lower MBE than the regional model, consistent with the validation results in Table 16.

4.1.13. UFS

Section A.15 shows the decomposition model equations for the UFS station. Table 17 shows the UFS station results. The localised, Cluster 2 and regional models outperform the baseline models. The Lee model underestimates the DNI slightly better than the Cluster 2 model.

Figure A15 shows the test results of the UFS dataset. All three new decomposition models significantly improve the errors compared to the baseline models, consistent with the validation results in Table 17.

Table 17. Hourly validation results of decomposition model development for UFS.

Model	Entire Dataset				$K_t < 0.60$	$K_t \geq 0.60$
	R^2	MBE [%]	RMSE [%]	MAE [%]	MAE [%]	MAE [%]
DISC	0.53	-18.0	38.7	31.7	61.8	23.4
Dirint	0.58	-26.4	40.0	33.0	63.6	24.6
Lee	0.6	-2.68	29.3	24.0	54.7	15.5
UFS	0.72	0.27	24.2	18.2	32.0	14.4
Cluster 2	0.73	-4.03	24.1	19.5	33.2	15.7
Regional	0.72	-1.79	23.9	19.0	33.4	15.1

4.1.14. UNV

Section A.16 shows the decomposition model equations for the UNV station. Table 18 shows the UNV station results. The localised, Cluster 2 and regional models significantly improved over the baseline models. The Cluster 2 and regional model overestimates the DNI more than the DISC model, based on the MBE.

Figure A16 shows the test results of the UNV dataset. The test results correspond with the validation results in Table 18, where the localised, Cluster 2 and regional models outperform the baseline models. The only exception is the MBE, where the Cluster 2 and regional models perform worse than the DISC model. Considering all the metrics, the new models outperform the baselines in reducing the overall error of DNI estimations.

Table 18. Hourly validation results of decomposition model development for UNV.

Model	Entire Dataset				$K_t < 0.60$	$K_t \geq 0.60$
	R^2	MBE [%]	RMSE [%]	MAE [%]	MAE [%]	MAE [%]
DISC	0.5	1.72	45.9	34.9	59.3	29.1
Dirint	0.56	-9.42	40.7	31.3	60.4	24.3
Lee	0.56	19.0	43.5	33.5	71.0	24.4
UNV	0.62	0.19	36.0	26.5	47.2	21.6
Cluster 2	0.61	7.05	37.3	25.9	47.1	20.8
Regional	0.62	10.1	37.8	26.1	47.0	21.1

4.1.15. UNZ

Section A.17 shows the decomposition model equations for the UNZ station. Table 19 shows the results of the UNZ station. The localised, clustered and regional models all show improvement over the baselines. The Dirint model has a lower MBE than the regional model.

Figure A17 shows the test results of the UNZ dataset, which correspond with the validation results in Table 19.

Preprints.org (www.preprints.org) | NOT PEER-REVIEWED | Posted: 7 March 2024 doi:10.20944/preprints202403.0416.v1

Table 19. Hourly validation results of decomposition model development for UNZ.

Model	Entire Dataset				$K_t < 0.60$	$K_t \geq 0.60$
	R^2	MBE [%]	RMSE [%]	MAE [%]	MAE [%]	MAE [%]
DISC	0.56	-0.21	41.6	32.0	58.7	24.4
Dirint	0.6	-11.9	38.2	29.5	59.9	20.9
Lee	0.6	13.5	38.2	30.2	64.7	20.3
UNZ	0.66	0.42	32.8	24.0	45.5	17.9
Cluster 3	0.66	0.13	33.0	24.1	45.9	17.9
Regional	0.68	3.56	32.3	23.8	44.7	17.9

4.1.16. UPR

Section A.18 shows the decomposition model equations for the UPR station. Table 20 shows the UPR station results. The localised, cluster and regional models outperform the baseline models.

Figure A18 shows the test results of the UPR dataset. The comparison metrics of the entire dataset indicate that the localised, cluster and regional models outperform the baseline models, which is consistent with the results of the validation dataset in Table 20.

Table 20. Hourly validation results of decomposition model development for UPR.

Model	Entire Dataset				$K_t < 0.60$	$K_t \geq 0.60$
	R^2	MBE [%]	RMSE [%]	MAE [%]	MAE [%]	MAE [%]
DISC	0.5	-15.2	40.6	33.3	61.0	25.5
Dirint	0.58	-24.0	39.7	32.1	61.3	23.9
Lee	0.61	2.48	29.9	24.7	55.2	16.1
UPR	0.71	-0.17	25.5	19.3	36.3	14.5
Cluster 2	0.71	-2.49	25.7	19.6	36.6	14.8
Regional	0.72	0.13	25.3	19.4	36.8	14.4

4.1.17. VAN

Section A.19 shows the decomposition model equations for the VAN station. Table 21 shows the results of the VAN station. The localised model outperforms the baseline models by improving R^2 and reducing the MBE, RMSE and MAE. The new models significantly reduce the MAE in the higher K_t compared to the baseline models. Even when outperforming the baseline models, the regional model performs the worst of the new model. The VAN station receives a very high average DNI and DHI and lower DHI than the rest of the database's stations. These results are similar to the RVD station, which has significantly higher irradiance levels than the other stations.

Figure A19 shows the test results of the VAN dataset. The new models all outperform the baseline models. The regional model shows the worst performance of the new models, even when outperforming the baseline models, similar to the RVD station that receives more irradiance on average compared to the other stations. These results are consistent with the validation results in Table 21.

Table 21. Hourly validation results of decomposition model development for VAN.

Model	Entire Dataset				$K_t < 0.60$	$K_t \geq 0.60$
	R^2	MBE [%]	RMSE [%]	MAE [%]	MAE [%]	MAE [%]
DISC	0.58	-11.3	32.2	25.3	60.6	17.9
Dirint	0.63	-21.0	33.6	27.5	62.7	20.1
Lee	0.64	-3.04	25.8	20.5	55.9	13.0
VAN	0.76	-1.17	20.9	15.7	35.2	11.6
Cluster 1	0.76	-1.57	20.9	15.9	36.3	11.7
Regional	0.75	-7.41	22.3	18.2	38.9	13.8

Preprints.org (www.preprints.org) | NOT PEER-REVIEWED | Posted: 7 March 2024 doi:10.20944/preprints202403.0416.v1

4.2. Discussion

Table 22 summarises the performance of the localised, clustered and regional models for both the test and validation sets.

As expected, the localised models outperformed the baseline models for all station datasets because of the site-specific climatic training data. As discussed in the previous section, the cluster model combines multiple stations in a similar geographical area.

The clustered model will have significantly more data from which to train a model. A clustered model is ideal if a site has no data for localised model development using the discussed methodology. The regional (Southern African) model also shows improvement over the baseline models, indicating that this model may be appropriate for adoption as a new model for Southern Africa. The two models with no localised model (ILA and MIN) showed improvement using the clustered and regional model in the validation study.

Table 22. Summary of test and validation sets of stations outperforming baseline models.

Dataset	Localised model outperforms baseline models		Cluster model outperforms baseline models		Regional model outperforms baseline models	
	Test	Validation	Test	Validation	Test	Validation
CSIR	✓	✓	✓	✓	✓	✓
CUT	✓	✓	✓	✓	✓	✓
FRH	✓	✓	✓	✓	✓	✓
GRT	✓	✓	✓	✓	✓	✓
HLO	✓	✓	✓	✓	✓	✓
ILA	-	✓	-	✓	-	✓
KZH	✓	✓	✓	✓	✓	✓
KZW	✓	✓	✓	✓	✓	✓
MIN	-	✓	-	✓	-	✓
NMU	✓	✓	✓	✓	✓	✓
NUST	✓	✓	✓	✓	✓	✓
RVD	✓	✓	✓	✓	✓	✓
SUN	✓	✓	✓	✓	✓	✓
UBG	✓	✓	✓	✓	✓	✓
UFS	✓	✓	✓	✓	✓	✓
UNV	✓	✓	✓	✓	✓	✓
UNZ	✓	✓	✓	✓	✓	✓
UPR	✓	✓	✓	✓	✓	✓
VAN	✓	✓	✓	✓	✓	✓

5. Conclusion

This article presented the development of a new decomposition model of hourly DNI estimations for Southern Africa. The new models improved the DISC model [17] in developing new decomposition models localised for Southern African climates. The new decomposition models improved the DNI estimation errors over the baselines for all validation and test sets.

The results indicate that a localised model will improve the estimations of DNI. The proposed methodology can be helpful for the development of local decomposition models for other areas worldwide.

Clustered models also indicate that grouping data based on similar geographical and climatic properties can also improve the performance of decomposition models. This phenomenon could be helpful when using a clustered decomposition model if no local model or limited data is available but from two or more geographically close stations.

The overall model, the regional decomposition model, is encapsulated by different climatic regions and geographical locations. There are also some exceptions where the model over- or underestimates

Preprints.org (www.preprints.org) | NOT PEER-REVIEWED | Posted: 7 March 2024 doi:10.20944/preprints202403.0416.v1

the DNI; however, the overall metrics indicate that the Southern African model significantly improves over the baseline models.

The study validates hourly irradiance data for K_t-intervals between 0.175 and 0.875. Recommendations for future work include developing models for higher and lower K_t values and models for higher temporal resolutions with increased accuracy, which is ideal for real-time monitoring and short-term forecasting of PV power.

Developing countries with an accurate decomposition model can open the path to expanding the use of renewable energy sources and reducing their dependence on coal and fossil fuels. Good-quality data is needed to ensure the progress of solar energy research and development. The next step is assessing the decomposition models with well-known transposition models to determine improved accuracy for PR estimations.

Author Contributions: Conceptualisation, F.D.; methodology, F.D.; software, F.D.; validation, F.D.; formal analysis, F.D.; investigation, F.D.; resources, F.D. and A.R.; data curation, F.D.; writing—original draft preparation, F.D.; writing—review and editing, F.D. and A.R.; visualisation, F.D.; supervision, A.R; project administration, F.D. and A.R; funding acquisition, F.D.and A.R. All authors have read and agreed to the published version of the manuscript.

Institutional Review Board Statement: Not applicable.

Informed Consent Statement: Not applicable.

Data Availability Statement: Not applicable.

Conflicts of Interest: The authors declare no conflict of interest.

Appendix A. Localised Decomposition Models

Appendix A.1. CSIR

The a, b and c coefficients for Equation (34) for the CSIR station are

$$
\begin{aligned}
a &= \begin{cases} 0.6472 - 1.0883K_t + 12.3429K_t^2 - 17.7027K_t^3 \text{ for } K_t < 0.60, \\ 6.1444 - 9.484K_t - 5.138K_t^2 + 9.2371K_t^3 \text{ for } K_t \geq 0.60. \end{cases} \\
b &= \begin{cases} -0.5032 + 5.67K_t - 22.0707K_t^2 + 22.2654K_t^3 \text{ for } K_t < 0.60, \\ 2.8669 - 22.2584K_t + 43.4833K_t^2 - 24.9682K_t^3 \text{ for } K_t \geq 0.60. \end{cases} \\
c &= \begin{cases} 0.1418 - 1.4904K_t + 4.7805K_t^2 - 4.3489K_t^3 \text{ for } K_t < 0.60, \\ -1.1287 + 5.8459K_t - 9.4568K_t^2 + 4.8729K_t^3 \text{ for } K_t \geq 0.60. \end{cases}
\end{aligned} \tag{A1}
$$

The test results of the CSIR dataset are in Figure A1.

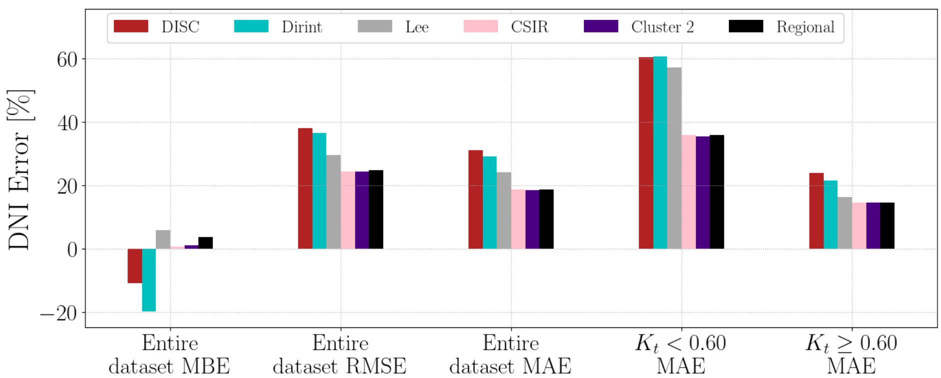

Figure A1. Hourly test results of decomposition model development for CSIR.

Appendix A.2. CUT

The a, b and c coefficients for Equation (34) for the CUT station are

$$a = \begin{cases} 2.4122 - 15.382K_t + 48.3773K_t^2 - 45.8766K_t^3 \text{ for } K_t < 0.60, \\ -15.7689 + 86.1878K_t - 141.6902K_t^2 + 73.2142K_t^3 \text{ for } K_t \geq 0.60. \end{cases}$$
$$b = \begin{cases} -1.6214 + 14.8897K_t - 45.5364K_t^2 + 40.6731K_t^3 \text{ for } K_t < 0.60, \\ 17.2881 - 85.5492K_t + 134.0146K_t^2 - 67.4052K_t^3 \text{ for } K_t \geq 0.60. \end{cases} \quad \text{(A2)}$$
$$c = \begin{cases} 0.2864 - 2.6906K_t + 7.8329K_t^2 - 6.7318K_t^3 \text{ for } K_t < 0.60, \\ -1.9147 + 9.6635K_t - 15.3053K_t^2 + 7.7563K_t^3 \text{ for } K_t \geq 0.60. \end{cases}$$

The validation results of the CUT dataset are in Figure A2.

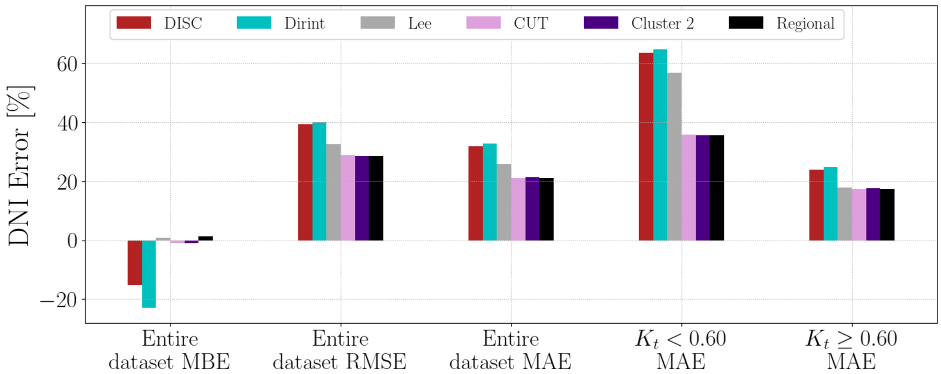

Figure A2. Hourly test results of decomposition model development for CUT.

Appendix A.3. FRH

The a, b and c coefficients for Equation (34) for the FRH station are

$$a = \begin{cases} 1.3199 - 6.0578K_t + 24.6953K_t^2 - 27.3825K_t^3 \text{ for } K_t < 0.60, \\ 33.3782 - 124.5221K_t + 155.5513K_t^2 - 64.7203K_t^3 \text{ for } K_t \geq 0.60. \end{cases}$$
$$b = \begin{cases} -0.5658 + 5.6247K_t - 21.3334K_t^2 + 21.2952K_t^3 \text{ for } K_t < 0.60, \\ -26.2959 + 102.0318K_t - 131.6271K_t^2 + 56.3592K_t^3 \text{ for } K_t \geq 0.60. \end{cases} \quad \text{(A3)}$$
$$c = \begin{cases} 0.0963 - 1.024K_t + 3.5042K_t^2 - 3.2887K_t^3 \text{ for } K_t < 0.60, \\ 3.9117 - 15.5175K_t + 20.4822K_t^2 - 8.9754K_t^3 \text{ for } K_t \geq 0.60. \end{cases}$$

The test results of the FRH dataset are in Figure A3.

Preprints.org (www.preprints.org) | NOT PEER-REVIEWED | Posted: 7 March 2024 doi:10.20944/preprints202403.0416.v1

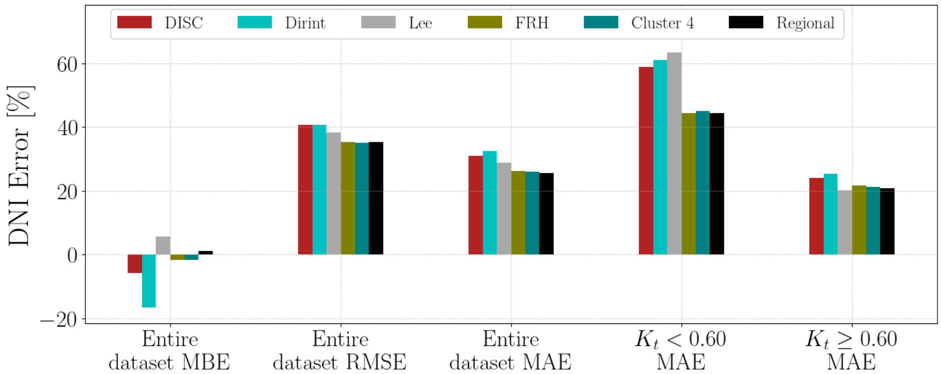

Figure A3. Hourly test results of decomposition model development for FRH.

Appendix A.4. GRT

The a, b and c coefficients for Equation (34) for the GRT station are

$$a = \begin{cases} 2.9602 - 19.6392K_t + 58.9738K_t^2 - 55.4505K_t^3 \text{ for } K_t < 0.60, \\ -29.0697 + 138.0498K_t - 209.2486K_t^2 + 102.455K_t^3 \text{ for } K_t \geq 0.60. \end{cases}$$
$$b = \begin{cases} -2.2843 + 20.1509K_t - 58.384K_t^2 + 51.362K_t^3 \text{ for } K_t < 0.60, \\ 34.8693 - 155.9554K_t + 227.6821K_t^2 - 108.7518K_t^3 \text{ for } K_t \geq 0.60. \end{cases} \tag{A4}$$
$$c = \begin{cases} 0.4656 - 4.1668K_t + 11.5129K_t^2 - 9.7101K_t^3 \text{ for } K_t < 0.60, \\ -8.4664 + 36.6029K_t - 51.9382K_t^2 + 24.2327K_t^3 \text{ for } K_t \geq 0.60. \end{cases}$$

Figure A4 shows the test results of the GRT dataset.

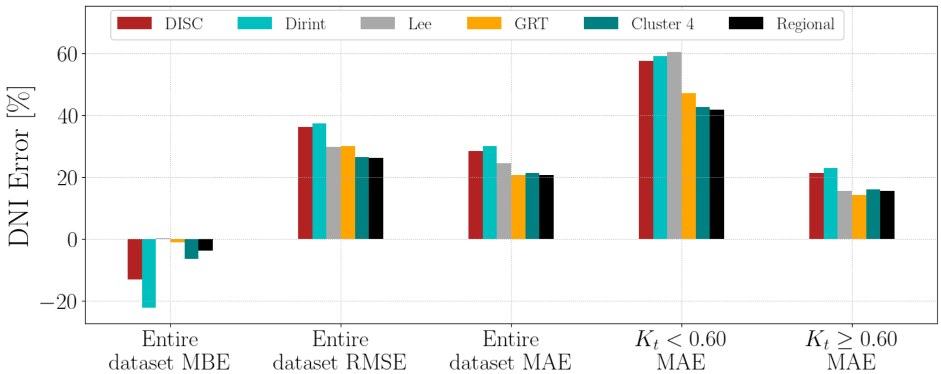

Figure A4. Hourly test results of decomposition model development for GRT.

Appendix A.5. HLO

The a, b and c coefficients for Equation (34) for the HLO station are

$$a = \begin{cases} 3.1156 - 21.0151K_t + 62.5312K_t^2 - 57.2369K_t^3 \text{ for } K_t < 0.60, \\ 50.8058 - 194.5525K_t + 248.2624K_t^2 - 105.3977K_t^3 \text{ for } K_t \geq 0.60. \end{cases}$$
$$b = \begin{cases} -2.0533 + 18.2104K_t - 53.4859K_t^2 + 46.7754K_t^3 \text{ for } K_t < 0.60, \\ -33.1822 + 128.4612K_t - 164.8983K_t^2 + 70.2185K_t^3 \text{ for } K_t \geq 0.60. \end{cases} \tag{A5}$$
$$c = \begin{cases} 0.3508 - 3.2108K_t + 9.1319K_t^2 - 7.7849K_t^3 \text{ for } K_t < 0.60, \\ 3.7247 - 14.4408K_t + 18.5853K_t^2 - 7.9382K_t^3 \text{ for } K_t \geq 0.60. \end{cases}$$

Figure A5 shows the test results of the HLO dataset.

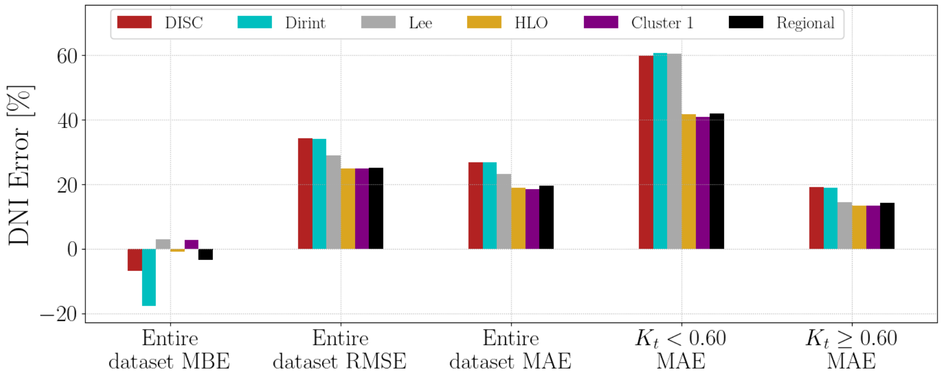

Figure A5. Hourly test results of decomposition model development for HLO.

Appendix A.6. ILA

There is no decomposition model developed for the ILA station.
The test results of the ILA dataset are in Figure A6.

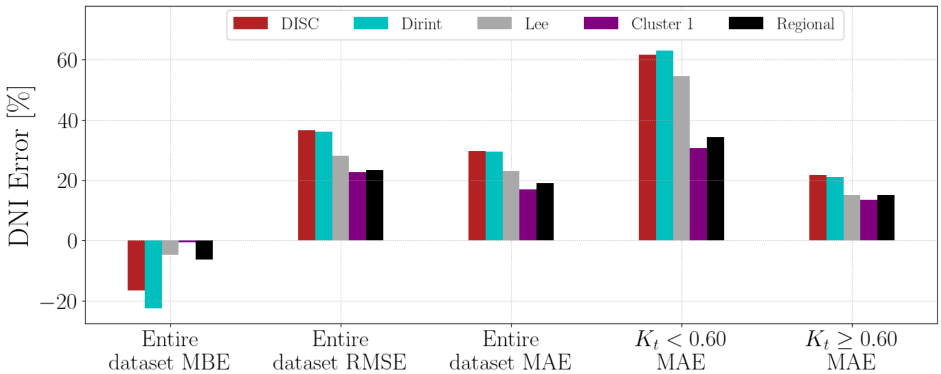

Figure A6. Hourly test results of decomposition model development for ILA.

Appendix A.7. KZH

The a, b and c coefficients for Equation (34) for the KZH station are

$$
\begin{aligned}
a &= \begin{cases} 1.3444 - 6.1333K_t + 23.7139K_t^2 - 25.5604K_t^3 \text{ for } K_t < 0.60, \\ 56.4073 - 216.3047K_t + 276.4264K_t^2 - 117.5281K_t^3 \text{ for } K_t \geq 0.60. \end{cases} \\
b &= \begin{cases} -0.7156 + 6.8854K_t - 24.0569K_t^2 + 22.9604K_t^3 \text{ for } K_t < 0.60, \\ -45.6353 + 178.5713K_t - 231.593K_t^2 + 99.6179K_t^3 \text{ for } K_t \geq 0.60. \end{cases} \\
c &= \begin{cases} 0.1646 - 1.6569K_t + 5.2451K_t^2 - 4.7368K_t^3 \text{ for } K_t < 0.60, \\ 6.2156 - 24.5162K_t + 32.0741K_t^2 - 13.9205K_t^3 \text{ for } K_t \geq 0.60. \end{cases}
\end{aligned} \quad \text{(A6)}
$$

The test results of the KZH dataset are in Figure A7.

Preprints.org (www.preprints.org) | NOT PEER-REVIEWED | Posted: 7 March 2024 doi:10.20944/preprints202403.0416.v1

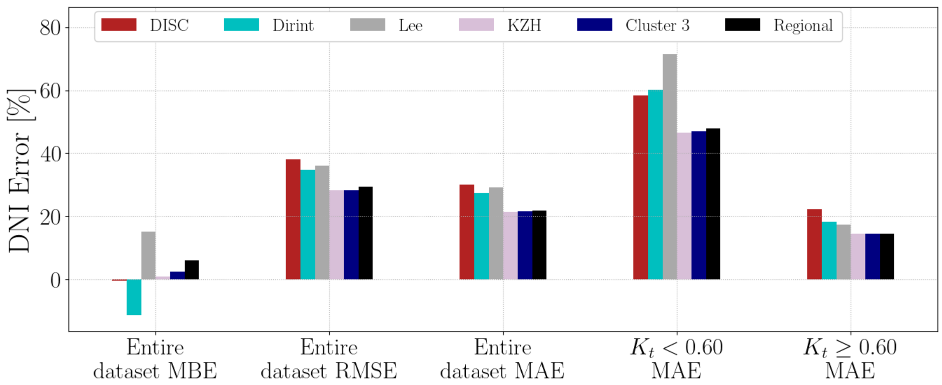

Figure A7. Hourly test results of decomposition model development for KZH.

Appendix A.8. KZW

The a, b and c coefficients for Equation (34) for the KZW station are

$$a = \begin{cases} 2.2627 - 14.4806K_t + 47.1629K_t^2 - 46.2386K_t^3 \text{ for } K_t < 0.60, \\ 35.0603 - 132.558K_t + 167.2728K_t^2 - 70.2359K_t^3 \text{ for } K_t \geq 0.60. \end{cases}$$
$$b = \begin{cases} -1.4332 + 13.4317K_t - 42.4822K_t^2 + 39.1838K_t^3 \text{ for } K_t < 0.60, \\ -28.1708 + 109.9004K_t - 141.9142K_t^2 + 60.6943K_t^3 \text{ for } K_t \geq 0.60. \end{cases} \quad \text{(A7)}$$
$$c = \begin{cases} 0.2678 - 2.6116K_t + 7.9363K_t^2 - 7.1072K_t^3 \text{ for } K_t < 0.60, \\ 3.1759 - 12.4602K_t + 16.1949K_t^2 - 6.9726K_t^3 \text{ for } K_t \geq 0.60. \end{cases}$$

Figure A8 shows the test results of the KZW dataset.

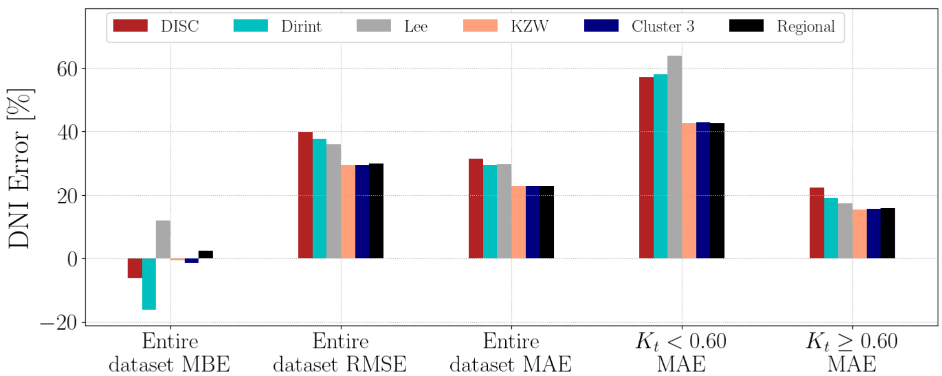

Figure A8. Hourly test results of decomposition model development for KZW.

Appendix A.9. MIN

There is no decomposition model developed for the MIN station.
The test results of the MIN dataset are in Figure A9.

Preprints.org (www.preprints.org) | NOT PEER-REVIEWED | Posted: 7 March 2024 doi:10.20944/preprints202403.0416.v1

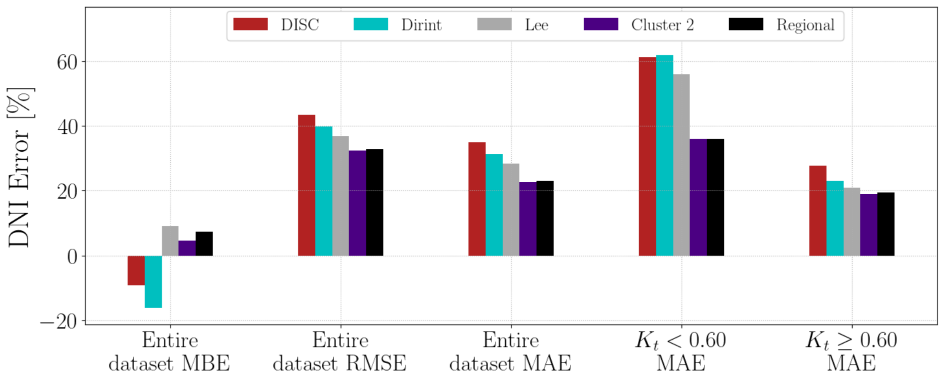

Figure A9. Hourly test results of decomposition model development for MIN.

Appendix A.10. NMU

The a, b and c coefficients for Equation (34) for the NMU station are

$$a = \begin{cases} 0.0688 + 5.2168K_t - 7.122K_t^2 + 0.2163K_t^3 \text{ for } K_t < 0.60, \\ 15.7683 - 48.8606K_t + 48.5956K_t^2 - 15.0438K_t^3 \text{ for } K_t \geq 0.60. \end{cases}$$
$$b = \begin{cases} 0.3483 - 2.9436K_t + 3.2778K_t^2 - 0.0145K_t^3 \text{ for } K_t < 0.60, \\ -11.0783 + 37.046K_t - 39.8763K_t^2 + 13.6687K_t^3 \text{ for } K_t \geq 0.60. \end{cases} \quad \text{(A8)}$$
$$c = \begin{cases} -0.0758 + 0.598K_t - 1.1265K_t^2 + 0.7025K_t^3 \text{ for } K_t < 0.60, \\ 1.9782 - 7.2272K_t + 8.7285K_t^2 - 3.4834K_t^3 \text{ for } K_t \geq 0.60. \end{cases}$$

The test results of the NMU dataset are in Figure A10.

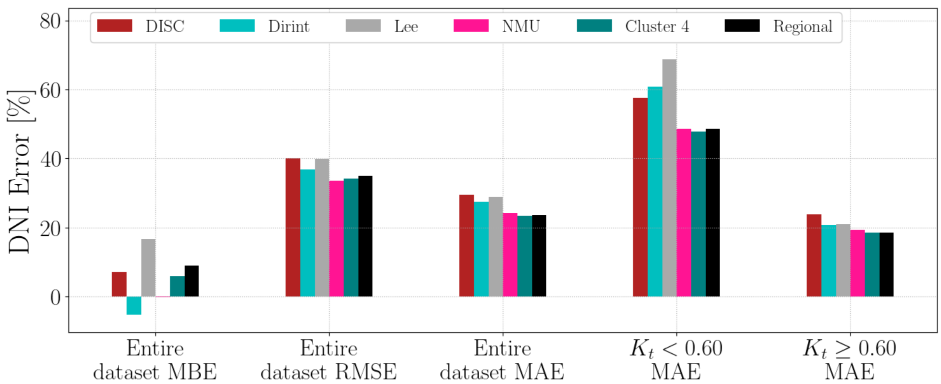

Figure A10. Hourly test results of decomposition model development for NMU.

Appendix A.11. NUST

The a, b and c coefficients for Equation (34) for the NUST station are

$$a = \begin{cases} 2.0021 - 11.1478K_t + 36.3216K_t^2 - 35.8544K_t^3 \text{ for } K_t < 0.60, \\ -17.9917 + 91.7087K_t - 144.5222K_t^2 + 72.3519K_t^3 \text{ for } K_t \geq 0.60. \end{cases}$$
$$b = \begin{cases} -1.2658 + 11.3567K_t - 35.6964K_t^2 + 32.4545K_t^3 \text{ for } K_t < 0.60, \\ 24.1237 - 111.1616K_t + 165.4905K_t^2 - 79.997K_t^3 \text{ for } K_t \geq 0.60, \end{cases} \quad \text{(A9)}$$
$$c = \begin{cases} 0.2056 - 1.9277K_t + 5.7745K_t^2 - 5.0518K_t^3 \text{ for } K_t < 0.60, \\ -2.59 + 11.8847K_t - 17.6199K_t^2 + 8.4894K_t^3 \text{ for } K_t \geq 0.60. \end{cases}$$

Preprints.org (www.preprints.org) | NOT PEER-REVIEWED | Posted: 7 March 2024 doi:10.20944/preprints202403.0416.v1

The test results of the NUST dataset are in Figure A11.

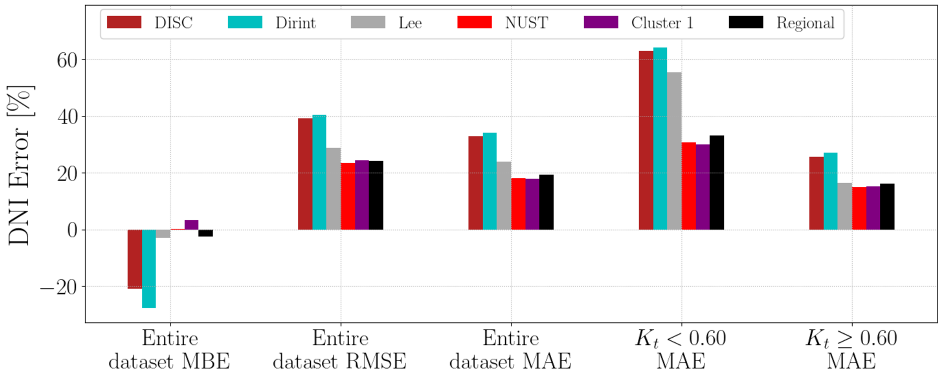

Figure A11. Hourly test results of decomposition model development for NUST.

Appendix A.12. RVD

The a, b and c coefficients for Equation (34) for the RVD station are

$$
\begin{aligned}
a &= \begin{cases} 4.0191 - 28.309K_t + 83.0024K_t^2 - 74.0684K_t^3 \text{ for } K_t < 0.60, \\ 84.2546 - 327.2114K_t + 422.3587K_t^2 - 181.2345K_t^3 \text{ for } K_t \geq 0.60. \end{cases} \\
b &= \begin{cases} -2.8895 + 25.4823K_t - 74.043K_t^2 + 63.2378K_t^3 \text{ for } K_t < 0.60, \\ -65.5943 + 256.2577K_t - 331.9301K_t^2 + 142.7166K_t^3 \text{ for } K_t \geq 0.60. \end{cases} \\
c &= \begin{cases} 0.5456 - 4.9199K_t + 13.8139K_t^2 - 11.415K_t^3 \text{ for } K_t < 0.60, \\ 10.4557 - 41.161K_t + 53.7847K_t^2 - 23.3378K_t^3 \text{ for } K_t \geq 0.60. \end{cases}
\end{aligned} \tag{A10}
$$

The test results of the RVD dataset are in Figure A12.

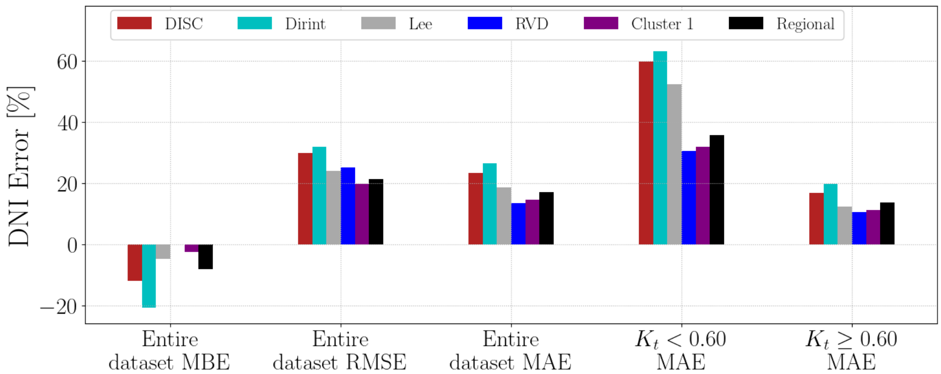

Figure A12. Hourly test results of decomposition model development for RVD.

Preprints.org (www.preprints.org) | NOT PEER-REVIEWED | Posted: 7 March 2024 doi:10.20944/preprints202403.0416.v1

Appendix A.13. SUN

The a, b and c coefficients for Equation (34) for the SUN station are

$$a = \begin{cases} 1.4996 - 7.646K_t + 30.0235K_t^2 - 33.6216K_t^3 \text{ for } K_t < 0.60, \\ 32.6225 - 122.3879K_t + 152.4023K_t^2 - 62.9667K_t^3 \text{ for } K_t \geq 0.60. \end{cases}$$
$$b = \begin{cases} -0.835 + 7.9823K_t - 28.5353K_t^2 + 28.4965K_t^3 \text{ for } K_t < 0.60, \\ -19.4403 + 73.2046K_t - 90.6277K_t^2 + 36.9662K_t^3 \text{ for } K_t \geq 0.60. \end{cases} \quad \text{(A11)}$$
$$c = \begin{cases} 0.1285 - 1.3014K_t + 4.3214K_t^2 - 4.0834K_t^3 \text{ for } K_t < 0.60, \\ 2.0866 - 7.7979K_t + 9.595K_t^2 - 3.8902K_t^3 \text{ for } K_t \geq 0.60. \end{cases}$$

The test results of the SUN dataset are in Figure A13.

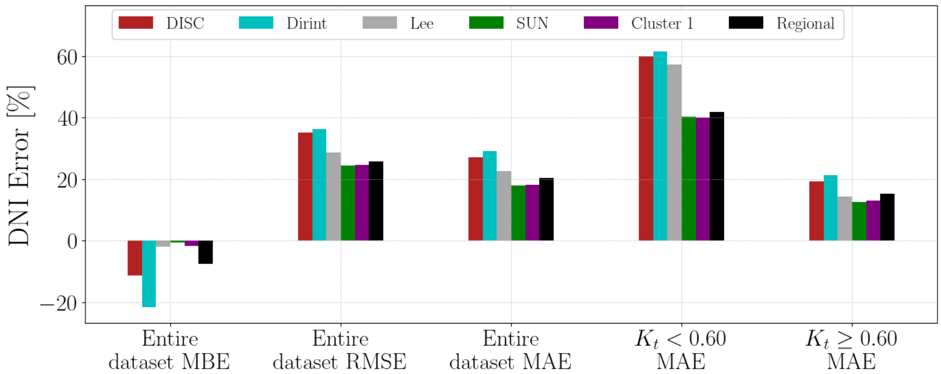

Figure A13. Hourly test results of decomposition model development for SUN.

Appendix A.14. UBG

The a, b and c coefficients for Equation (34) for the UBG station are

$$a = \begin{cases} 0.5601 + 1.4348K_t + 1.9992K_t^2 - 6.4178K_t^3 \text{ for } K_t < 0.60, \\ 42.1623 - 152.8269K_t + 183.6564K_t^2 - 73.01K_t^3 \text{ for } K_t \geq 0.60. \end{cases}$$
$$b = \begin{cases} -0.0378 + 0.6077K_t - 6.2716K_t^2 + 7.0084K_t^3 \text{ for } K_t < 0.60, \\ -44.4913 + 167.9403K_t - 209.5344K_t^2 + 86.5114K_t^3 \text{ for } K_t \geq 0.60. \end{cases} \quad \text{(A12)}$$
$$c = \begin{cases} 0.0159 - 0.2605K_t + 1.1245K_t^2 - 0.8877K_t^3 \text{ for } K_t < 0.60, \\ 9.2841 - 35.956K_t + 46.1639K_t^2 - 19.6586K_t^3 \text{ for } K_t \geq 0.60. \end{cases}$$

The test results of the SUN dataset are in Figure A14.

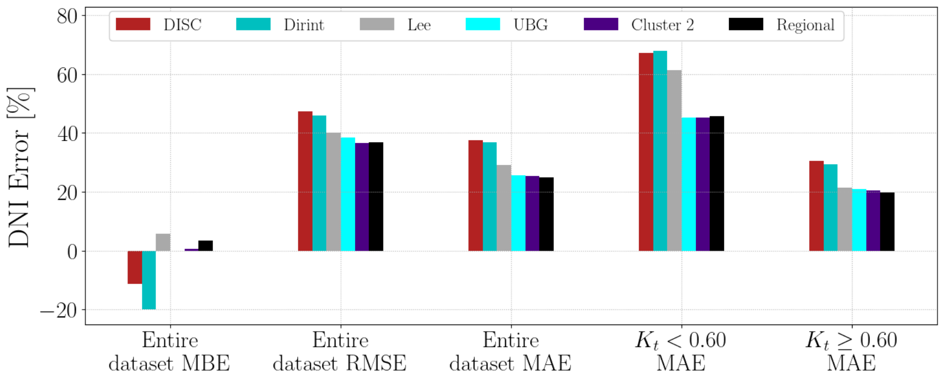

Figure A14. Hourly test results of decomposition model development for UBG.

Appendix A.15. UFS

The a, b and c coefficients for Equation (34) for the UFS station are

$$a = \begin{cases} 1.1152 - 5.4355K_t + 27.3687K_t^2 - 32.6276K_t^3 \text{ for } K_t < 0.60, \\ 18.8962 - 58.0528K_t + 56.4791K_t^2 - 16.8735K_t^3 \text{ for } K_t \geq 0.60. \end{cases}$$
$$b = \begin{cases} -0.5439 + 6.5875K_t - 27.7113K_t^2 + 28.8812K_t^3 \text{ for } K_t < 0.60, \\ -19.1711 + 65.1123K_t - 71.8324K_t^2 + 25.6916K_t^3 \text{ for } K_t \geq 0.60. \end{cases} \quad \text{(A13)}$$
$$c = \begin{cases} 0.1395 - 1.6147K_t + 5.7356K_t^2 - 5.4904K_t^3 \text{ for } K_t < 0.60, \\ 5.238 - 19.7369K_t + 24.6715K_t^2 - 10.2415K_t^3 \text{ for } K_t \geq 0.60. \end{cases}$$

The test results of the SUN dataset are in Figure A15.

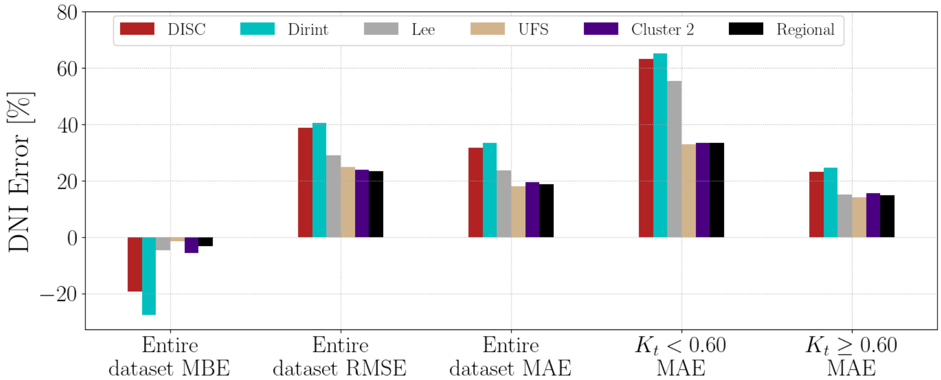

Figure A15. Hourly test results of decomposition model development for UFS.

Appendix A.16. UNV

The a, b and c coefficients for Equation (34) for the UNV station are

$$a = \begin{cases} 1.6679 - 8.8496K_t + 30.8258K_t^2 - 31.7801K_t^3 \text{ for } K_t < 0.60, \\ 17.0947 - 58.7362K_t + 67.3532K_t^2 - 25.6036K_t^3 \text{ for } K_t \geq 0.60. \end{cases}$$
$$b = \begin{cases} -0.9329 + 8.8795K_t - 29.6546K_t^2 + 28.1554K_t^3 \text{ for } K_t < 0.60, \\ -11.0559 + 39.0859K_t - 45.1859K_t^2 + 17.0921K_t^3 \text{ for } K_t \geq 0.60. \end{cases} \quad \text{(A14)}$$
$$c = \begin{cases} 0.1744 - 1.744K_t + 5.4271K_t^2 - 4.9023K_t^3 \text{ for } K_t < 0.60, \\ 0.7738 - 2.5106K_t + 2.5888K_t^2 - 0.8303K_t^3 \text{ for } K_t \geq 0.60. \end{cases}$$

Preprints.org (www.preprints.org) | NOT PEER-REVIEWED | Posted: 7 March 2024 doi:10.20944/preprints202403.0416.v1

The test results of the UNV dataset are in Figure A16.

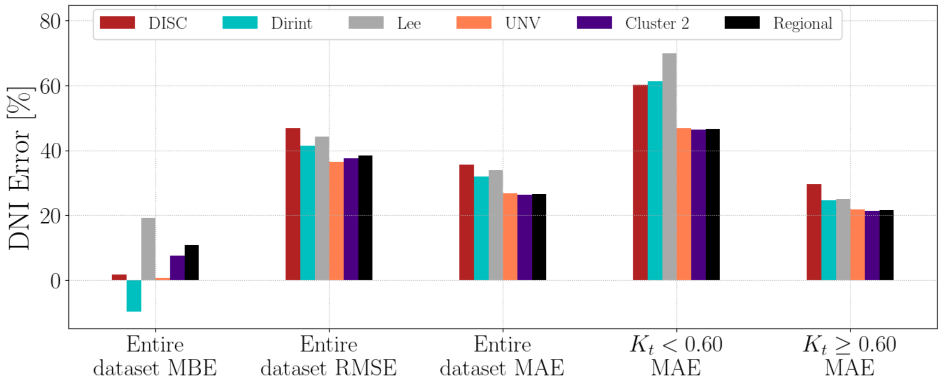

Figure A16. Hourly test results of decomposition model development for UNV.

Appendix A.17. UNZ

The a, b and c coefficients for Equation (34) for the UNZ station are

$$a = \begin{cases} 1.1129 - 5.2859K_t + 25.5284K_t^2 - 30.5998K_t^3 \text{ for } K_t < 0.60, \\ 33.4179 - 127.1391K_t + 161.8637K_t^2 - 68.7679K_t^3 \text{ for } K_t \geq 0.60. \end{cases}$$
$$b = \begin{cases} -0.6222 + 7.0597K_t - 28.1112K_t^2 + 29.4187K_t^3 \text{ for } K_t < 0.60, \\ -24.1838 + 94.1721K_t - 121.4204K_t^2 + 51.9098K_t^3 \text{ for } K_t \geq 0.60. \end{cases} \tag{A15}$$
$$c = \begin{cases} 0.1398 - 1.5931K_t + 5.5902K_t^2 - 5.4749K_t^3 \text{ for } K_t < 0.60, \\ 2.3838 - 9.2877K_t + 11.9991K_t^2 - 5.1432K_t^3 \text{ for } K_t \geq 0.60. \end{cases}$$

The test results of the UNZ dataset are in Figure A17.

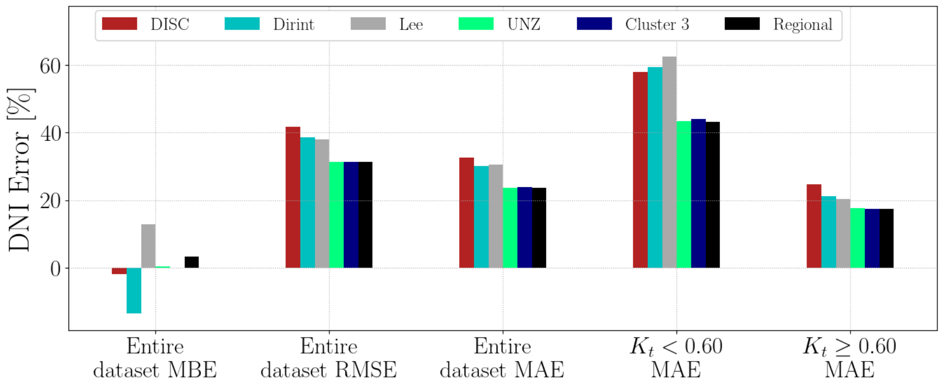

Figure A17. Hourly test results of decomposition model development for UNZ.

Appendix A.18. UPR

The a, b and c coefficients for Equation (34) for the UPR station are

$$a = \begin{cases} 1.3766 - 6.4439K_t + 25.7243K_t^2 - 28.9372K_t^3 \text{ for } K_t < 0.60, \\ -2.5908 + 24.5466K_t - 49.3217K_t^2 + 28.3294K_t^3 \text{ for } K_t \geq 0.60. \end{cases}$$
$$b = \begin{cases} -0.8308 + 8.2061K_t - 29.0534K_t^2 + 28.667K_t^3 \text{ for } K_t < 0.60, \\ 9.0641 - 45.9866K_t + 73.7132K_t^2 - 37.7903K_t^3 \text{ for } K_t \geq 0.60. \end{cases} \quad (A16)$$
$$c = \begin{cases} 0.1626 - 1.6496K_t + 5.2698K_t^2 - 4.8501K_t^3 \text{ for } K_t < 0.60, \\ -1.7989 + 8.4045K_t - 12.7021K_t^2 + 6.2414K_t^3 \text{ for } K_t \geq 0.60. \end{cases}$$

The test results of the UPR dataset are in Figure A18.

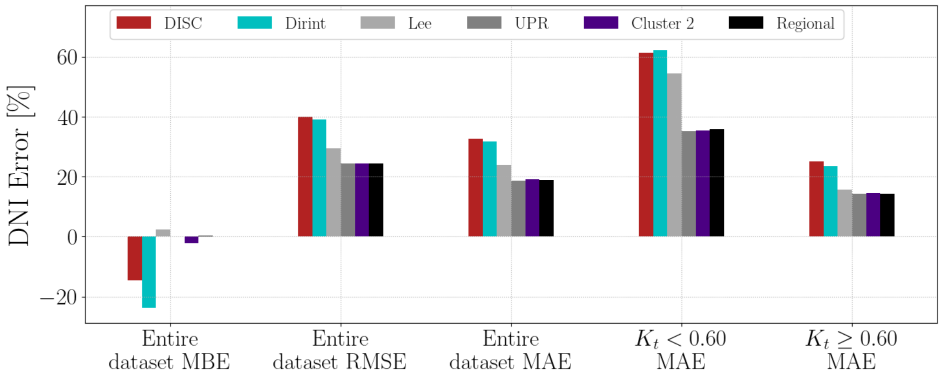

Figure A18. Hourly test results of decomposition model development for UPR.

Appendix A.19. VAN

The a, b and c coefficients for Equation (34) for the VAN station are

$$a = \begin{cases} 1.8649 - 12.2743K_t + 47.2823K_t^2 - 50.5904K_t^3 \text{ for } K_t < 0.60, \\ 7.6031 - 11.9134K_t - 6.9687K_t^2 + 12.3734K_t^3 \text{ for } K_t \geq 0.60. \end{cases}$$
$$b = \begin{cases} -1.1265 + 12.1632K_t - 44.5245K_t^2 + 44.4602K_t^3 \text{ for } K_t < 0.60, \\ 3.6296 - 27.7921K_t + 54.161K_t^2 - 31.162K_t^3 \text{ for } K_t \geq 0.60. \end{cases} \quad (A17)$$
$$c = \begin{cases} 0.2277 - 2.5008K_t + 8.4732K_t^2 - 8.0774K_t^3 \text{ for } K_t < 0.60, \\ -1.3247 + 7.0528K_t - 11.5818K_t^2 + 6.025K_t^3 \text{ for } K_t \geq 0.60. \end{cases}$$

Figure A19 shows the test results of the VAN dataset.

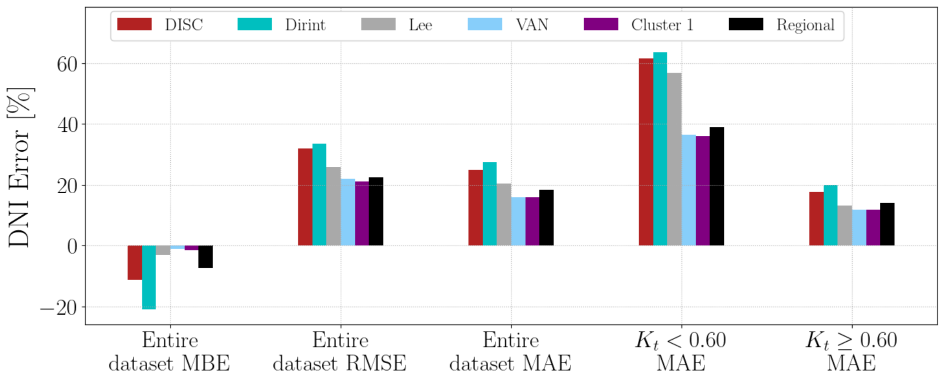

Figure A19. Hourly test results of decomposition model development for VAN.

References

1. Masters, G. *Renewable and Efficient Electric Power Systems*, 2 ed.; John Wiley and Sons, Inc.: Hoboken, New Jersey, 2013; pp. 186–245,316–398.
2. Sengupta, M.; Habte, A.; Wilbert, S.; Gueymard, C.; Remund, J. Best Practices Handbook for the Collection and Use of Solar Resource Data for Solar Energy Applications: Third Edition **2021**. doi:https://dx.doi.org/10.2172/1778700.
3. Lee, H.; Kim, S.Y.; Yun, C. Comparison of Solar Radiation Models to Estimate Direct Normal Irradiance for Korea. *Energies* **2017**, *10*, 594. doi:10.3390/en10050594.
4. Bertrand, C.; Vanderveken, G.; Journée, M. Evaluation of decomposition models of various complexity to estimate the direct solar irradiance over Belgium. *Renewable Energy* **2015**, *74*, 618 – 626. doi:https://doi.org/10.1016/j.renene.2014.08.042.
5. Liu, B.Y.; Jordan, R.C. The interrelationship and characteristic distribution of direct, diffuse and total solar radiation. *Solar Energy* **1960**, *4*, 1 – 19. doi:https://doi.org/10.1016/0038-092X(60)90062-1.
6. Yang, D.; Gueymard, C.A. Ensemble model output statistics for the separation of direct and diffuse components from 1-min global irradiance. *Solar Energy* **2020**, *208*, 591–603. doi:https://doi.org/10.1016/j.solener.2020.05.082.
7. Boland, J.; Huang, J.; Ridley, B. Decomposing global solar radiation into its direct and diffuse components. *Renewable and Sustainable Energy Reviews* **2013**, *28*, 749–756. doi:https://doi.org/10.1016/j.rser.2013.08.023.
8. Ridley, B.; Boland, J.; Lauret, P. Modelling of diffuse solar fraction with multiple predictors. *Renewable Energy* **2010**, *35*, 478–483. doi:https://doi.org/10.1016/j.renene.2009.07.018.
9. Soares, J.; Oliveira, A.P.; Božnar, M.Z.; Mlakar, P.; Escobedo, J.F.; Machado, A.J. Modeling hourly diffuse solar-radiation in the city of São Paulo using a neural-network technique. *Applied Energy* **2004**, *79*, 201–214. doi:https://doi.org/10.1016/j.apenergy.2003.11.004.
10. Talvitie, T.; Eldali, F.; Pinney, D. Predicting Solar Diffuse and Direct Components Using Deep Neural Networks. *2021 IEEE Power & Energy Society Innovative Smart Grid Technologies Conference (ISGT)* **2021**, pp. 1–5.
11. Kalyanam, R.; Hoffmann, S. A Novel Approach to Enhance the Generalization Capability of the Hourly Solar Diffuse Horizontal Irradiance Models on Diverse Climates. *Energies* **2020**, *13*. doi:10.3390/en13184868.
12. Bessafi, M.; Oree, V.; Khoodaruth, A.; Chabriat, J.P. Impact of decomposition and kriging models on the solar irradiance downscaling accuracy in regions with complex topography. *Renewable Energy* **2020**, *162*, 1992–2003. doi:https://doi.org/10.1016/j.renene.2020.10.018.
13. Janjai, S.; Phaprom, P.; Wattan, R.; Masiri, I. Statistical models for estimating hourly diffuse solar radiation in different regions of Thailand. Proceedings of the International Conference on Energy and Sustainable Development: Issues and Strategies (ESD 2010), 2010, pp. 1–6. doi:10.1109/ESD.2010.5598771.
14. Orgill, J.; Hollands, K. Correlation equation for hourly diffuse radiation on a horizontal surface. *Solar Energy* **1977**, *19*, 357 – 359. doi:https://doi.org/10.1016/0038-092X(77)90006-8.
15. Erbs, D.; Klein, S.; Duffie, J. Estimation of the diffuse radiation fraction for hourly, daily and monthly-average global radiation. *Solar Energy* **1982**, *28*, 293 – 302. doi:https://doi.org/10.1016/0038-092X(82)90302-4.

16. Louche, A.; Notton, G.; Poggi, P.; Simonnot, G. Correlations for direct normal and global horizontal irradiation on a French Mediterranean site. *Solar Energy (Journal of Solar Energy Science and Engineering); (USA)* **1991**, *46*. doi:10.1016/0038-092X(91)90072-5.
17. Maxwell, E. A quasi-physical model for converting hourly global horizontal to direct normal insolation. Technical report, Solar Energy Research Institute, 1987.
18. Perez, R.; Ineichen, P.; Maxwell, E.; Seals, R.; Zelenka, A. Dynamic global-to-direct irradiance conversion models. *ASHRAE Transactions* **1992**, *98*, 354–369.
19. Lave, M.; Hayes, W.; Pohl, A.; Hansen, C.W. Evaluation of Global Horizontal Irradiance to Plane-of-Array Irradiance Models at Locations Across the United States. *IEEE Journal of Photovoltaics* **2015**, *5*, 597–606.
20. Lee, K.; Yoo, H.; Levermore, G.J. Quality control and estimation hourly solar irradiation on inclined surfaces in South Korea. *Renewable Energy* **2013**, *57*, 190 – 199. doi:https://doi.org/10.1016/j.renene.2013.01.028.
21. Skartveit, A.; Olseth, J.A. A model for the diffuse fraction of hourly global radiation. *Solar Energy* **1987**, *38*, 271 – 274. doi:https://doi.org/10.1016/0038-092X(87)90049-1.
22. Lam, J.C.; Li, D.H. Correlation between global solar radiation and its direct and diffuse components. *Building and Environment* **1996**, *31*, 527 – 535. doi:https://doi.org/10.1016/0360-1323(96)00026-1.
23. Reindl, D.; Beckman, W.; Duffie, J. Diffuse Fraction Correlations. *Solar Energy* **1990**, *45*, 1–7. doi:10.1016/0038-092X(90)90060-P.
24. Yao, W.; Li, Z.; Xiu, T.; Lu, Y.; Li, X. New decomposition models to estimate hourly global solar radiation from the daily value. *Solar Energy* **2015**, *120*, 87–99. doi:https://doi.org/10.1016/j.solener.2015.05.038.
25. Khalil, S.A.; Shaffie, A. A comparative study of total, direct and diffuse solar irradiance by using different models on horizontal and inclined surfaces for Cairo, Egypt. *Renewable and Sustainable Energy Reviews* **2013**, *27*, 853–863. doi:https://doi.org/10.1016/j.rser.2013.06.038.
26. Gueymard, C.A.; Ruiz-Arias, J.A. Extensive worldwide validation and climate sensitivity analysis of direct irradiance predictions from 1-min global irradiance. *Solar Energy* **2016**, *128*, 1–30. Special issue: Progress in Solar Energy, doi:https://doi.org/10.1016/j.solener.2015.10.010.
27. Laiti, L.; Giovannini, L.; Zardi, D.; Belluardo, G.; Moser, D. Estimating Hourly Beam and Diffuse Solar Radiation in an Alpine Valley: A Critical Assessment of Decomposition Models. *Atmosphere* **2018**, *9*. doi:10.3390/atmos9040117.
28. Oliveira, A.P.; Escobedo, J.; Machado, A.; Soares, J. Correlation models of diffuse solar-radiation applied to the city of São Paulo, Brazil. *Applied Energy* **2002**, *71*, 59–73. doi:https://doi.org/10.1016/S0306-2619(01)00040-X.
29. Salazar, G.; Pedrosa Filho, M. Analysis of the Diffuse Fraction from Solar Radiation Values Measured in Argentina and Brazil Sites. 2020. doi:10.18086/swc.2019.44.05.
30. Chendo, M.; Maduekwe, A. Hourly global and diffuse radiation of Lagos, Nigeria—Correlation with some atmospheric parameters. *Solar Energy* **1994**, *52*, 247–251. doi:https://doi.org/10.1016/0038-092X(94)90491-X.
31. Chikh, M.; Mahrane, A.; Haddadi, M. Modeling the Diffuse Part of the Global Solar Radiation in Algeria. *Energy Procedia* **2012**, *18*, 1068–1075. Terragreen 2012: Clean Energy Solutions for Sustainable Environment (CESSE), doi:https://doi.org/10.1016/j.egypro.2012.05.121.
32. Benchrifa, M.; Tadili, R.; Idrissi, A.; Essalhi, H.; Mechaqrane, A. Development of New Models for the Estimation of Hourly Components of Solar Radiation: Tests, Comparisons, and Application for the Generation of a Solar Database in Morocco. *International Journal of Photoenergy* **2021**, *2021*, 1–16. doi:10.1155/2021/8897818.
33. Engerer, N. Minute resolution estimates of the diffuse fraction of global irradiance for southeastern Australia. *Solar Energy* **2015**, *116*, 215–237. doi:https://doi.org/10.1016/j.solener.2015.04.012.
34. Tsubo, M.; Walker, S. Relationships between photosynthetically active radiation and clearness index at Bloemfontein, South Africa. *Theoretical and Applied Climatology* **2005**, *80*, 17–25. doi:10.1007/s00704-004-0080-5.
35. Nijegorodov, N. Improved ashrae model to predict hourly and daily solar radiation components in Botswana, Namibia, and Zimbabwe. *Renewable Energy* **1996**, *9*, 1270–1273. World Renewable Energy Congress Renewable Energy, Energy Efficiency and the Environment, doi:https://doi.org/10.1016/0960-1481(96)88508-9.

 doi:10.20944/preprints202403.0416.v1

36. Mabasa, B.; Lysko, M.D.; Tazvinga, H.; Zwane, N.; Moloi, S.J. The Performance Assessment of Six Global Horizontal Irradiance Clear Sky Models in Six Climatological Regions in South Africa. *Energies* **2021**, *14*. doi:10.3390/en14092583.
37. Mahachi, T. Energy yield analysis and evaluation of solar irradiance models for a utility scale solar PV plant in South Africa. Master's thesis, University of Stellenbosch, South Africa, 2016.
38. Daniel, F.M.; Rix, A.J. The Evaluation of Decomposition Models Under Varying Weather Conditions for South Africa. Southern African Sustainable Energy Conference, 2021, pp. 207–213.
39. SAURAN. https://sauran.ac.za/, 2022.
40. Daniel-Durandt, F.M.; Rix, A.J. Automating Quality Control of Irradiance Data with a Comprehensive Analysis for Southern Africa. *Solar* **2023**, *3*, 596–617. doi:10.3390/solar3040032.
41. Walpole, R.; Myers, R.; Myers, S.; Ye, K. *Probability & Statistics for Engineers & Scientists*; Pearson Education Inc.: Boston, MA, 2012.
42. Anaconda Software Distribution, 2020.
43. Holmgren, W.; Hansen, C.; Mikofski, M. pvlib python: a python package for modeling solar energy systems. *Journal of Open Source Software* **2018**, *3*, 884. doi:10.21105/joss.00884.
44. McKinney, W.; others. Data structures for statistical computing in python. Proceedings of the 9th Python in Science Conference. Austin, TX, 2010, Vol. 445, pp. 51–56.
45. Hunter, J.D. Matplotlib: A 2D graphics environment. *Computing in Science & Engineering* **2007**, *9*, 90–95. doi:10.1109/MCSE.2007.55.
46. Mahachi, T.; Rix, A. Evaluation of irradiance decomposition and transposition models for a region in South Africa Investigating the sensitivity of various diffuse radiation models. IECON 2016 - 42nd Annual Conference of the IEEE Industrial Electronics Society, 2016, pp. 3064–3069. doi:10.1109/IECON.2016.7793897.
47. Kasten, F.; Young, A.T. Revised optical air mass tables and approximation formula. *Appl. Opt.* **1989**, *28*, 4735–4738. doi:10.1364/AO.28.004735.
48. Farmer, W.; Rix, A.J. Mapping the spatial perturbations seen by the power system network due to intermittent renewable energy sources. Southern African Sustainable Energy Conference, 2021, pp. 222–228.
49. Solargis. https://solargis.com/maps-and-gis-data/download/south-africa, 2021.